Combustion and Flame 168 (2016) 342–364

Contents lists available at ScienceDirect

Combustion and Flame

journal homepage: www.elsevier.com/locate/combustflame

Degree of Disequilibrium analysis for automatic selection of kinetic constraints in the Rate-Controlled Constrained-Equilibrium method☆

Gian Paolo Beretta[a,*], Mohammad Janbozorgi[b], Hameed Metghalchi[c]

[a] Università di Brescia, Brescia, Italy
[b] University of California Los Angeles, Los Angeles, CA, United States
[c] Northeastern University, Boston, MA, United States

ARTICLE INFO

Article history:
Received 25 August 2015
Revised 2 February 2016
Accepted 2 February 2016
Available online 22 March 2016

Keywords:
Model order reduction in chemical kinetics
Non-equilibrium thermodynamics
Rate-Controlled Constrained-Equilibrium (RCCE) method
Chemical relaxation

ABSTRACT

The Rate-Controlled Constrained-Equilibrium (RCCE) model reduction scheme for chemical kinetics provides acceptable accuracies with a number of differential equations much lower than the number of species in the underlying Detailed Kinetic Model (DKM). To yield good approximations, however, the method requires accurate identification of the rate controlling constraints. So far, a drawback of the RCCE scheme has been the absence of a fully automatable and systematic procedure that is capable of identifying the best constraints for a given range of thermodynamic conditions and a required level of approximation. In this paper, we propose a new methodology for such identification based on a simple algebraic analysis of the results of a preliminary simulation of the underlying DKM, which is focused on the behaviour of the degrees of disequilibrium (DoD) of the individual chemical reactions. The new methodology is based on computing an Approximate Reduced Row Echelon Form of the Actual Degrees of Disequilibrium (ARREFADD) with respect to a preset tolerance level. An alternative variant is to select an Approximate Singular Value Decomposition of the Actual Degrees of Disequilibrium (ASVDADD). Either procedure identifies a low dimensional subspace in the DoD space, from which the actual DoD traces do not depart beyond a fixed distance related to the preset tolerance (ARREFADD methodology) or to the first neglected singular value of the matrix of DoD traces (ASVDADD methodology). The effectiveness and robustness of the method is demonstrated for the case of a very rapid supersonic nozzle expansion of the products of hydrogen and methane oxycombustion and for the case of methane/oxygen ignition. The results are in excellent agreement with DKM predictions. For both variants of the method, we provide a simple Matlab code implementing the proposed constraint selection algorithm.

1. Introduction

According to the Rate-Controlled Constrained-Equilibrium (RCCE) theory, the reactions in a Detailed Kinetic Model (DKM) can be characterized in terms of the effectiveness with which they contribute to the spontaneous tendency to relax the composition towards chemical equilibrium. Loosely speaking, such effectiveness depends on the number of "kinetic bottlenecks" that the reaction needs to go through in order to advance and on how "narrow" these bottlenecks are. Each kinetic bottleneck is characterized by a linear combination of the composition, called a "constraint", which can be varied only by reactions that go through that particular bottleneck. Therefore, the "narrower" the bottleneck, the slower the rate of change of the associated rate-limiting constraint.

The general idea behind the RCCE method [1–14] is that for each particular problem, set of conditions, and acceptable degree of approximation there is a threshold time scale which essentially separates the "relatively fast" equilibrating kinetic mechanisms from those that slow down and control the spontaneous relaxation towards equilibrium. The "relatively slow" mechanisms control the interesting part of the non-equilibrium dynamics in that they effectively identify a low dimensional manifold in composition space, where, for the chosen level of approximation, the dynamics can be assumed to take place. In general, the rate controlling mechanisms are slow because they have to go through one or more bottlenecks. For example, the three-body reactions are slow because they

☆ The authors wish to dedicate this paper to the memory of the brilliant founder of the rate-controlled constrained-equilibrium theory and their mentor, teacher, and coauthor, the late professor James C. Keck of the Massachussetts Institute of Technology, whose biography and scientific production is available at www.JamesKeckCollectedWorks.org.

* Corresponding author. Fax: +39 0303702448.
E-mail addresses: gianpaolo.beretta@unibs.it (G.P. Beretta), mjanbozorgi@gmail.com (M. Janbozorgi), metghalchi@coe.neu.edu (H. Metghalchi).

http://dx.doi.org/10.1016/j.combustflame.2016.02.005
0010-2180/

Nomenclature

$\boldsymbol{a} = [a_{ij}] = [a_{i1}, \ldots, a_{in_{sp}}]$	matrix of constraint coefficients
$A_\ell = RT\phi_\ell = -\sum_{j=1}^{n_{sp}} \nu_{j\ell}\mu_j$	de-Donder affinity of reaction ℓ
A_ℓ^+, b_ℓ^+, E_ℓ^+	prefactor, temperature exponent, and activation energy of the forward rate constant of reaction ℓ
$c_i(\mathbf{N}) = \sum_{j=1}^{n_{sp}} a_{ij}N_j$	ith constraint functional of the composition vector $\mathbf{N}$
$\mathrm{coker}(\boldsymbol{\nu})$	left null space (co-kernel) of matrix $\boldsymbol{\nu}$, often called the *inhert subspace*
$\mathrm{DoD}_\ell = \phi_\ell = \ln(r_\ell^+/r_\ell^-)$	Degree of Disequilibrium of reaction ℓ, the same as ϕ_ℓ
$g_{jj}(T,p) = \mu_{jj}(T,p)$	Gibbs free energy of pure substance j at pressure p and temperature T (double subscript denotes pure substance)
$\Delta g_\ell^o(T) = \sum_{j=1}^{n_{sp}} \nu_{j\ell} g_{jj}(T,p_o)$	Gibbs free energy of reaction ℓ at standard pressure p_o and temperature T
I_{sp}	nozzle thrust force per unit mass flow rate of the propellant
$k_\ell^+(T)$	forward rate constant of reaction ℓ at temperature T
$k_\ell^-(T)$	backward rate constant of reaction at temperature
$K_\ell^{co}(T)$	equilibrium constant (based on concentration) of reaction ℓ at temperature T
$[N_j]$	concentration of species j
$N = \sum_{j=1}^{n_{sp}} N_j$	total number of moles
$\mathbf{N} = [N_1 \ \ldots \ N_{n_{sp}}]$	vector of species mole numbers
p, p_o	pressure, atmospheric pressure
r_ℓ^+	forward rate of reaction ℓ
r_ℓ^-	reverse rate of reaction ℓ
R	universal gas constant
$\mathrm{span}(\{\boldsymbol{\nu}_\ell\})$	column space of the stoichiometric matrix $\boldsymbol{\nu}$ i.e., linear span of the set of vectors defined by its columns, often called the *reactive subspace*
T	temperature
$X_j = N_j/N$	mole fraction of species j
$\boldsymbol{X} = [X_1 \ \ldots \ X_{n_{sp}}]$	vector of species mole fractions
$\ln(\boldsymbol{X}) = [\ln(X_1) \ldots \ln(X_{n_{sp}})]$	vector of logarithms of the species mole fractions

Greek symbols

γ_i	constraint potential, i.e., Lagrange multiplier associated with the i-th constraint
$\lambda_j = -\mu_j/RT$	entropic chemical potential of species j
$\boldsymbol{\Lambda} = [\lambda_1 \ \ldots \ \lambda_{n_{sp}}]$	vector of entropic chemical potentials
$\boldsymbol{\Lambda}_\perp$	component of the row vector $\boldsymbol{\Lambda}$ orthogonal to span $(\{\boldsymbol{\nu}_\ell\})$
$\boldsymbol{\Lambda}_{\mathrm{DoD}} = \boldsymbol{\Lambda} - \boldsymbol{\Lambda}_\perp$	vector that we call Overall Degree of Disequilibrium
$\boldsymbol{\Lambda}_{\mathrm{DoD}}(z_p) = \boldsymbol{U\Sigma V^T}$	singular value decomposition of the $n_{sp} \times P$ matrix $\boldsymbol{\Lambda}_{\mathrm{DoD}}(Z_p)$
$\mu_j = \mu_{j,\mathrm{off}}(T,p,\mathbf{N})$	chemical potential of species j in a non-reacting mixture of "frozen" composition $\mathbf{N}$ (hence the "off" subscript) in stable equilibrium at temperature T and pressure p
$\nu_{j\ell}^+$	forward stoichiometric coefficient of species j in reaction ℓ
$\nu_{j\ell}^-$	reverse stoichiometric coefficient of species j in reaction ℓ
$\nu_{j\ell} = \nu_{j\ell}^- - \nu_{j\ell}^+$	net stoichiometric coefficient of species j in reaction ℓ
$\boldsymbol{\nu} = [\nu_{j\ell}]$	matrix of stoichiometric coefficients
$\boldsymbol{\nu}_\ell = [\nu_{1\ell} \ \ldots \ \nu_{n_{sp}\ell}]$	vector of the stoichiometric coefficients of reaction ℓ, defined by the ℓ-th column of the matrix $\boldsymbol{\nu}$ of stoichiometric coefficients
$\phi_\ell = \ln(r_\ell^+/r_\ell^-) = \langle \boldsymbol{\Lambda} \vert \boldsymbol{\nu}_\ell \rangle$	Degree of Disequilibrium of reaction ℓ, same as DoD_ℓ
$\boldsymbol{\chi}_k = [\chi_{1k} \ \ldots \ \chi_{n_{sp}k}]$	a basis for $(\{\boldsymbol{\nu}_\ell\})$

Acronyms

ARREFADD	Approximate Reduced Row Echelon Form of the Actual Degrees of Disequilibrium
ASVDADD	Approximate Singular Value Decomposition of the Actual Degrees of Disequilibrium
DKM	Detailed Kinetic Model
DoD	Degree of Disequilibrium
RCCE	Rate-Controlled Constrained-Equilibrium

require three-body collisions which occur much less frequently than two-body collisions. As a result, the bottleneck mechanism is that of three-body collisions and the associated rate-limiting constraint is the total number of moles, which would not change if all three-body reactions were frozen. The "narrowness" of each bottleneck can be measured by the characteristic time with which the associated constraint would relax towards its equilibrium value in the absence of interactions sustaining the non-equilibrium state.

As emphasized for example in Ref. [12], the RCCE method enjoys a very appealing built-in general feature of strong thermodynamic consistency. However, the main difficulties in its practical use have been: (a) identifying the kinetic bottlenecks and (b) constructing an efficient set of constraints implied by them. Several efforts have addressed these problems with varying degrees of success [15]. The Greedy algorithm [16] and its extension including local improvements [17] select, one at a time, the most effective single-species constraints by cyclic execution of the DKM. This approach has shown to be efficient for turbulent flames in conjunction with in situ adaptive tabulation. Level of Importance (LOI) [18] picks up single species as constraints from the top of the list of species which are sorted based on their time scales. The method has demonstrated acceptable agreements with DKM calculations. Nonetheless, as shown in [17], time-scale based methods for the selection of constraints do not necessarily identify the most effective set of constraints. The analysis of the DoD traces of all the chemical reactions obtained from a full DKM calculation was shown in Ref. [19] to provide important information for selecting constraints. However, it ultimately fell short to be fully rationalized and automated for a general case. It is the aim of this paper to present a methodology to fully rationalize the idea presented in [19], regardless of the complexity of the mechanism, in a truly algorithmic manner. The proposed methodology, therefore, holds the promise to resolve the difficulties involved with the lack of a systematic way to choose constraints, which has long represented the main obstacle toward a widespread use of the RCCE method.

Currently, several reduction techniques populate the current state of the art about methods to simplify complex chemical kinetics modelling for a variety of applications. Quasi-Steady State Approximation (QSSA) [20] is commonly applied to species which react on a short time scale compared to other species and are, therefore, expected to be in a steady state. Their corresponding rate equations are then replaced with algebraic equations. Intrinsic Low-Dimensional Manifold (ILDM) [21] and Computational Singular Perturbation method (CSP) [22,23] use a dynamical systems approach of time scale analysis to reduce the stiffness in the model equations. ILDM tries to identify systematically the species for which the QSSA holds and CSP tries to eliminate the contribution of the so-called locally exhausted modes [23] to the evolution of species. In a later extension of CSP [24], a procedure was developed to discard elementary reactions and species that are deemed unimportant to the fast and slow dynamics, thereby developing a skeletal mechanism from the detailed model. In techniques based on adaptive chemistry [25–27], the low dimensional manifold is tabulated in the form of an entire library of locally accurate, reduced kinetic models at different compositions and temperatures that have been preliminarily proved to approximate the full chemistry reasonably well. A great deal of effort has thus been devoted to developing methods for reducing the size of the underlying DKM. In addition to those already mentioned, the followings are most notable: Partial Equilibrium Approximation [28], Directed Relation Graph (DRG) [29], ICE-PIC method [30], Method of Invariant Manifolds [31], and skeletal scheme reduction based on level of importance [32] or entropy production [33].

In this paper, the idea discussed in [19] is first pursued and rationalized to a level that results in a smaller, yet equally effective set of constraints. Then, further inspection of that idea opens the stage to define a fully systematic algorithm for constraint identification. To fix ideas and demonstrate the higher efficiency of the proposed methodology, the nozzle configuration of [19] is used also here. We analyse the Degree of Disequilibrium (DoD) data generated by a DKM simulation and show how they provide clear indications on what constraints are associated with the physical bottlenecks that are effectively in control of the kinetics. Then, when the structure of the DoD traces is complex and the grouping of reactions cannot be obtained by simple inspection, we show that the logic of our methodology can be still implemented by computing the Approximate Reduced Row Echelon Form of the Actual Degrees of Disequilibrium (ARREFADD) with respect to a preset tolerance level. Geometrically, this procedure identifies the lowest dimensional subspace in DoD space from which the actual DoD traces do not depart beyond a fixed distance related to the preset tolerance. This provides a systematic, fully automatable and simple algorithm for constraint identification capable of generating the optimal set of RCCE constraints for each preset level of approximation.

The effectiveness of the proposed algorithm, as well as of its variant based on computing the Approximate Singular Value Decomposition of the Actual Degrees of Disequilibrium (ASVDADD), is demonstrated here for a few case studies of increasing complexity. A full validation study as well as a study of the relations between the present method and the state of the art reduction methods that populate the literature [19–23] are beyond our scope here and will be presented elsewhere.

To help develop appreciation for the rationale of the new method, the first part of the article (Sections 2–5) – which an expert in model order reduction could skip or glance through – starts from the analysis of a simple particular case. This enables building up useful heuristics that allow grasping the more abstract linear algebra and basic observations from which we derive the new method in the second part that deals with the general case. Therefore, the article is organized as follows. Section 2 discusses the supersonic diverging nozzle set-up, the assumed hydrogen oxy-combustion DKM, and the findings of [19] which constitute the preliminary background for our additional observations, presented in Sections 3 and 4. Section 5 outlines the new constraint selection methodology for a case in which the reaction grouping can be done by simple inspection of the DoD traces, and demonstrates its efficiency and remarkable predictive ability by means of comparisons against a full DKM simulation and the methodology of [19]. Section 6 introduces additional fundamental observations and notation that constitute the geometrical basis for the ARREFADD method, finally presented in Section 7. Section 8 introduces the powerful ASVDADD variant of the method. Section 9 demonstrates the validity of the new methodology for other examples of nozzle and channel flows of increasing complexity. Section 10 concludes that the new method resolves the difficulties that prevented so far the RCCE method from widespread use. Appendices A and B provide a simple MatLab implementation of the proposed ARREFADD and ASVDADD algorithms, respectively. Appendix C summarizes the vector space notation used in the paper.

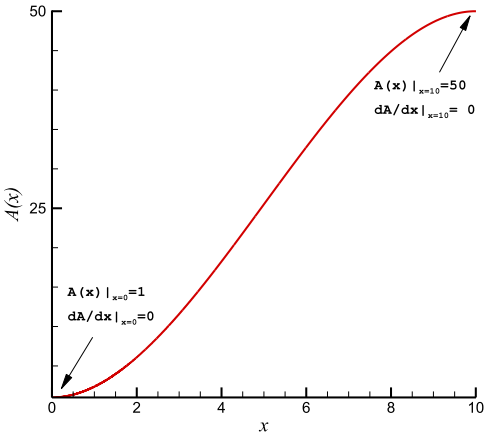

Fig. 1. Dimensionless cross sectional area $A(x)$ of the diverging nozzle considered in [19]. The exit-to-throat area ratio is 50 and the nozzle length is 10 times the diameter of the throat section. At the throat, the inlet flow is sonic based on frozen Mach number, the temperature is 3000 K, the pressure 25 atm, and the mixture is assumed at chemical equilibrium. The residence time is 3.7 ms.

2. Physical model and problem formulation

The set-up of interest is one that was also considered in [19]. It involves supersonic relaxation of combustion products within a diverging nozzle with an area profile as shown in Fig. 1. The nozzle has an exit-to-throat area ratio of 50 and a length 10 times the diameter of the throat section. The dimensionless coordinate x denotes the ratio of the centerline downstream distance from the throat to the throat diameter. The dimensionless area $A(x)$ denotes the ratio of nozzle cross sectional area to throat area. At the throat the inlet flow conditions are just above sonic based on frozen Mach number. Temperature and pressure at the throat are 3000 K and 25 atm, respectively, and the mixture is assumed to be at chemical equilibrium. The residence time within the nozzle is 3.7 ms.

Table 1 shows the 24 reactions of the Hydrogen/Oxygen DKM assumed here and in [19]. It also shows the parameters that determine the forward reaction rate constants

$$k_\ell^+(T) \;=\; A_\ell^+ T^{b_\ell^+} \exp(-E_\ell^+/RT) \tag{1}$$

in mol-cm-s-K units with the forward activation energy E_ℓ^+ in cal/mol. The backward reaction rate constants are determined from the principle of detailed balance,

$$k_\ell^-(T) = k_\ell^+(T)/K_\ell^{\rm co}(T) \tag{2}$$

Table 1
The 24 reactions of the hydrogen/oxygen Detailed Kinetic Model (DKM) considered in [19] and in the present study, together with the parameters that determine the forward reaction rate constants via equation $k_\ell^+(T) = A_\ell^+ T^{b_\ell^+} \exp(-E_\ell^+/RT)$ and the transpose of the matrix $\boldsymbol{\nu} = [\nu_{j\ell}]$ of stoichiometric coefficients.

					Species: j =	1	2	3	4	5	6	7	8
						O	O_2	H	H_2	OH	H_2O	HO_2	H_2O_2
ℓ	Reaction ℓ	A_ℓ^+	b_ℓ^+	E_ℓ^+		$\nu_{1\ell}$	$\nu_{2\ell}$	$\nu_{3\ell}$	$\nu_{4\ell}$	$\nu_{5\ell}$	$\nu_{6\ell}$	$\nu_{7\ell}$	$\nu_{8\ell}$
1	$O+O+M=O_2+M$	1.20E+17	−1	0	$\boldsymbol{\nu}_1 = [$	−2	1	0	0	0	0	0	0]
2	$O+H+M=OH+M$	5.00E+17	−1	0	$\boldsymbol{\nu}_2 = [$	−1	0	−1	0	1	0	0	0]
3	$H+H+M=H_2+M$	1.00E+18	−1	0	$\boldsymbol{\nu}_3 = [$	0	0	−2	1	0	0	0	0]
4	$H+H+H_2=H_2+H_2$	9.00E+16	−0.6	0	$\boldsymbol{\nu}_4 = [$	0	0	−2	1	0	0	0	0]
5	$H+H+H_2O=H_2+H_2O$	6.00E+19	−1.3	0	$\boldsymbol{\nu}_5 = [$	0	0	−2	1	0	0	0	0]
6	$H+OH+M=H_2O+M$	2.20E+22	−2	0	$\boldsymbol{\nu}_6 = [$	0	0	−1	0	−1	1	0	0]
7	$H+O_2+M=HO_2+M$	2.80E+18	−0.9	0	$\boldsymbol{\nu}_7 = [$	0	−1	−1	0	0	0	1	0]
8	$H+O_2+O_2=HO_2+O_2$	2.08E+19	−1.2	0	$\boldsymbol{\nu}_8 = [$	0	−1	−1	0	0	0	1	0]
9	$H+O_2+H_2O=HO_2+H_2O$	1.13E+19	−0.8	0	$\boldsymbol{\nu}_9 = [$	0	−1	−1	0	0	0	1	0]
10	$OH+OH+M=H_2O_2+M$	7.40E+13	−0.4	0	$\boldsymbol{\nu}_{10} = [$	0	0	0	0	−2	0	0	1]
11	$O+H_2=H+OH$	3.87E+04	2.7	6260	$\boldsymbol{\nu}_{11} = [$	−1	0	1	−1	1	0	0	0]
12	$O+HO_2=OH+O_2$	2.00E+13	0	0	$\boldsymbol{\nu}_{12} = [$	−1	1	0	0	1	0	−1	0]
13	$O+H_2O_2=OH+HO_2$	9.63E+06	2	4000	$\boldsymbol{\nu}_{13} = [$	−1	0	0	0	1	0	1	−1]
14	$H+O_2=O+OH$	2.65E+16	−0.7	17,041	$\boldsymbol{\nu}_{14} = [$	1	−1	−1	0	1	0	0	0]
15	$H+HO_2=O+H_2O$	3.97E+12	0	671	$\boldsymbol{\nu}_{15} = [$	1	0	−1	0	0	1	−1	0]
16	$H+HO_2=O_2+H_2$	4.48E+13	0	1068	$\boldsymbol{\nu}_{16} = [$	0	1	−1	1	0	0	−1	0]
17	$H+HO_2=OH+OH$	8.40E+13	0	635	$\boldsymbol{\nu}_{17} = [$	0	0	−1	0	2	0	−1	0]
18	$H+H_2O_2=HO_2+H_2$	1.21E+07	2	5200	$\boldsymbol{\nu}_{18} = [$	0	0	−1	1	0	0	1	−1]
19	$H+H_2O_2=OH+H_2O$	1.00E+13	0	3600	$\boldsymbol{\nu}_{19} = [$	0	0	−1	0	1	1	0	−1]
20	$OH+H_2=H+H_2O$	2.16E+08	1.5	3430	$\boldsymbol{\nu}_{20} = [$	0	0	1	−1	−1	1	0	0]
21	$OH+OH=O+H_2O$	3.57E+04	2.4	−2110	$\boldsymbol{\nu}_{21} = [$	1	0	0	0	−2	1	0	0]
22	$OH+HO_2=O2+H_2O$	1.45E+13	0	−500	$\boldsymbol{\nu}_{22} = [$	0	1	0	0	−1	1	−1	0]
23	$OH+H_2O_2=HO_2+H_2O$	2.00E+12	0	427	$\boldsymbol{\nu}_{23} = [$	0	0	0	0	−1	1	1	−1]
24	$HO_2+HO_2=O_2+H_2O_2$	1.30E+11	0	−1630	$\boldsymbol{\nu}_{24} = [$	0	1	0	0	0	0	−2	1]

where

$$K_\ell^{co}(T) = \left(\frac{p_o}{RT}\right)^{\nu_\ell} \exp\left(-\frac{\Delta g_\ell^o(T)}{RT}\right) \tag{3}$$

is the reaction equilibrium constant (based on concentration). Also, $\nu_\ell = \sum_j \nu_{j\ell}$, $\nu_{j\ell} = \nu_{j\ell}^- - \nu_{j\ell}^+$, where $\nu_{j\ell}^+$ and $\nu_{j\ell}^-$ are the forward and reverse stoichiometric coefficients of the ℓth reaction, respectively, and $\Delta g_\ell^o(T) = \sum_{j=1}^{n_{sp}} \nu_{j\ell} g_{jj}(T, p_o)$ is the Gibbs free energy of the ℓth reaction at standard pressure p_o and temperature T, where $g_{jj} = \mu_{jj}$ (with the double subscript) refers to the Gibbs free energy of pure substance j. In the present paper, we use the notation of [4], which differs only slightly from that of [19]. The symbol $g_j = \mu_i$ (with a single subscript), used below, represents instead the partial Gibbs free energy, i.e., the chemical potential, of species j in the mixture.

The Degree of Disequilibrium of reaction ℓ, ϕ_ℓ, is defined as follows:

$$\phi_\ell = \ln\left(r_\ell^+ / r_\ell^-\right) \tag{4}$$

where r_ℓ^+ and r_ℓ^- are the forward and reverse reaction rates, respectively, defined as

$$r_\ell^+ = k_\ell^+(T) \prod_{j=1}^{n_{sp}} \left[N_j\right]^{\nu_{j\ell}^+} \text{ and } r_\ell^- = k_\ell^-(T) \prod_{j=1}^{n_{sp}} \left[N_j\right]^{\nu_{j\ell}^-} \tag{5}$$

where n_{sp} is the number of species in the kinetic model. For convenience of the discussion below, we denote the Degree of Disequilibrium of a reaction also by DoD_ℓ or simply DoD. Figure 2 shows for all 24 reactions how the respective DoDs evolve along the axis of the diverging nozzle as the temperature drops rapidly due to the supersonic expansion. Clearly, the DoDs are not sign definite and by reversing a reaction in the DKM the corresponding DoD changes sign. For example, in Fig. 2 reactions 11 and 14 exhibit (very small) negative DoDs.

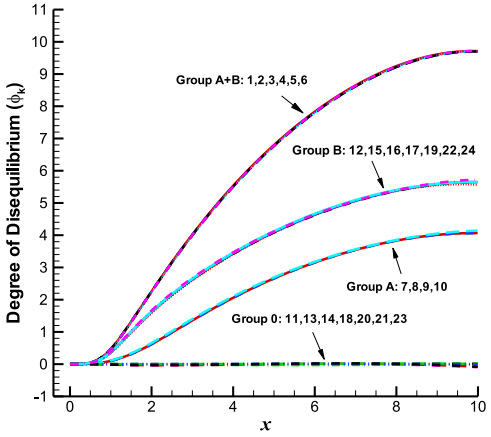

Fig. 2. Degrees of disequilibrium, $\phi_\ell = \ln(r_\ell^+/r_\ell^-)$, of the 24 reactions of Table 1 plotted versus the dimensionless downstream coordinate x along the nozzle axis, obtained (as in [19]) from a DKM simulation for the conditions detailed in Fig. 1. Reactions 11 and 14 exhibit (very small) negative DoDs.

It is worth noticing that the DoD of reaction ℓ is related to its de-Donder affinity, $A_\ell = -\sum_{j=1}^{n_{sp}} \nu_{j\ell}\mu_j$, as follows:

$$\phi_\ell = \frac{A_\ell}{RT} = -\frac{1}{RT}\sum_{j=1}^{n_{sp}} \nu_{j\ell}\mu_j \tag{6}$$

where $\mu_j = \mu_{j,\text{off}}(T, p, \mathbf{N})$ is the chemical potential of species j in the so-called "surrogate system" [34,35], namely, the non-reacting mixture (hence the "off" subscript) at stable thermodynamic equilibrium with the same temperature T, pressure p, and composition $\mathbf{N}$ as the actual non-equilibrium state of the reacting mixture.

The mathematical interpretation of Eq. (6) is that the DoD of a reaction is a linear combination of the rows of the stoichiometric matrix, with $-\mu_j/RT$ as the coefficients of the linear combination. This means that if some columns of the stoichiometric matrix are linearly dependent, then so are the corresponding DoDs. In other words, one could mathematically prove that, if there exists a set

of coefficients α_ℓ such that $\sum_{\ell=1}^{n_r} \nu_{j\ell}\alpha_\ell = 0$ for every j, then, by Eq. (6), we also have $\sum_{\ell=1}^{n_r} \phi_\ell\alpha_\ell = 0$.

Finally, the non-equilibrium law of mass action for reaction ℓ can be shown to relate to its DoD as follows (combine Eqs. (110) and (112) of [4])

$$\prod_{j=1}^{n_{sp}} \left[N_j\right]^{\nu_{j\ell}} = K_\ell^{\rm co}(T)\exp(-\phi_\ell) \tag{7}$$

At the throat, all reactions are at equilibrium, i.e., $\phi_\ell = 0$ for every ℓ. Downstream, the quick change in nozzle area causes a decrease in temperature, rapid enough to prevent the slow reactions from remaining near equilibrium and, hence, their DoDs build up as the fluid elements move downstream.

In the physical problem which we examine for illustrative purposes, it is assumed that full chemical equilibrium holds at the entrance (throat) of the nozzle. Such a condition is not encountered frequently in reacting flow configurations, but it turns out to serve well our purpose in the first part of the paper to explain the rather compelling numerical evidence about the underlying physics that emerges from the DoD analysis of the simple nozzle example. This example provides strong heuristic motivation for the proposed general algorithm.

In the second part of the paper, the application of the proposed methodology is demonstrated for the more challenging problem of homogeneous ignition of a stoichiometric mixture of methane and oxygen in a constant-area plug-flow reactor. The flow velocity is small enough (Ma = 0.0001) that the flow remains subsonic throughout the channel and reaches complete chemical equilibrium before exiting.

3. Preliminary observations about DoDs in the underlying DKM

The main observation in [19] is that the plots in Fig. 2 show clearly that for the given nozzle geometry and flow conditions every reaction in the group 11-13-14-18-20-21-23, that we refer to as "Group 0", maintains an approximately vanishing DoD throughout the nozzle. This means that these reactions are able to equilibrate quickly, in the sense that their DoDs remain very close to zero all along the nozzle. Therefore, on the time scale of interest for the given nozzle geometry and flow conditions, these reactions are not slowed down by any of the kinetic bottlenecks which control the spontaneous relaxation towards chemical equilibrium. In other words, the constraints associated with the controlling bottlenecks are not directly affected by the advancement of any of these reactions.

We denote constraint functionals of the composition vector **N** as follows:

$$c_i(\mathbf{N}) = \sum_{j=1}^{n_{sp}} a_{ij}N_j \tag{8}$$

where the constraint matrix $\boldsymbol{a} = [a_{ij}]$ plays a crucial role in the RCCE method. Recalling that $\dot{N}_j = \sum_{\ell=1}^{n_r} \nu_{j\ell}(r_\ell^+ - r_\ell^-)$, the rates of change of the constraint functionals under the DKM are given by

$$\dot{c}_i = \sum_{j=1}^{n_{sp}} a_{ij} \sum_{\ell=1}^{n_r} \nu_{j\ell}\left(r_\ell^+ - r_\ell^-\right) = \sum_{\ell=1}^{n_r} b_{i\ell}\left(r_\ell^+ - r_\ell^-\right) \tag{9}$$

where n_r is the number of reactions in the DKM and

$$b_{i\ell} = \sum_{j=1}^{n_{sp}} a_{ij}\nu_{j\ell} \tag{10}$$

represents the contribution of the net rate of reaction ℓ to the rate of change of constraint functional $c_i(\mathbf{N})$.

In order for constraint functional c_i to be unaffected directly by the net rate of reaction ℓ it is necessary and sufficient that $b_{i\ell}$ be zero, or at least very small. Geometrically, this means that the i-th row of the constraint matrix a_{ij} is orthogonal to the ℓth column of the stoichiometric matrix $\nu_{j\ell}$. This orthogonality condition is automatically satisfied for the two rows $a_{{\rm H}j}$ and $a_{{\rm O}j}$ of the constraint matrix a_{ij} that represent the number of atomic nuclei of hydrogen and oxygen, respectively. This is because $b_{{\rm H}\ell}$ and $b_{{\rm O}\ell}$ are zero for every reaction ℓ in the DKM, as required by the physical constraint of conservation of atomic nuclei in chemical reactions. Similarly, the fact that reactions in "Group 0" have vanishing DoDs requires that the rows of the constraint matrix $\boldsymbol{a} = [a_{ij}]$ corresponding to every constraint (bottleneck) which effectively controls the dynamics, must be orthogonal to the columns 11-13-14-18-20-21-23 of the stoichiometric matrix $\boldsymbol{\nu} = [\nu_{j\ell}]$.

The above observation is shown in [19] to provide an important clue for the selection of constraints. There, according to the traditional RCCE approach [1–8], constraints are assumed to be linear combinations of a set of known physically meaningful constraints, listed in Table 2, namely, EH (total number of hydrogen nuclei), EO (total number of oxygen nuclei), M (total number of moles), FV (free valence), FO (free oxygen), and a few others. The fact that a constraint must not be affected by the (two-body) reactions 11-13-14-18-20-21-23 provides a strong condition that when integrated with well-educated chemical kinetic reasoning and analysis of the DKM, can be exploited, as in [19], to come up with a good semi-empirical choice of a set of governing RCCE constraints. Indeed, very good approximation of the full H/O DKM results have been obtained in [19] using RCCE with a set of only three constraints (M, FO, FV) in addition to the two required by conservation of atomic elements (EH, EO).

Despite its remarkable performance, however, the analysis presented in [19] to construct constraints cannot be claimed to be "systematic", as the authors made note of some contradictory information implied by one or few reactions in formulating the constraints. It is the aim of the next section to devise a mathematical approach that fully rationalizes the constraint selection for this problem.

4. Additional observations about DoDs in the underlying DKM

The main observation that we put forward in this section and on which we elaborate in the rest of the paper, is that, in addition to the "equilibrated reactions" (those with approximately zero DoDs, i.e., zero affinity), the non-zero DoDs in Fig. 2 also carry additional information that is equally important for constraint selection. Obviously, they partition the reactions with non-zero DoDs into three other groups of reactions that to a high degree of approximation share at every downstream position x the same value of DoD. Indeed, as already shown in [19] and discussed in the previous section, important indications can be extracted from the DoD = 0 group (the group of equilibrated reactions). However, the fact that when pulled out of equilibrium at a particular rate the reactions turn out to bin themselves into one of a small number of groups characterized by levels of DoD shared exactly or approximately by all reactions in the group, provides additional indications that allow to fully pin down the governing constraints.

While the DoD = 0 "Group 0" identifies several possible constraints, each of the other groups, which appears to be characterized by a common relaxation time, furnishes (by analogous inspection) tighter indications useful to identify the rate-controlling bottlenecks of the overall kinetic mechanism that are effective at such time scale. To be more specific, the fact that Fig. 2 shows for each downstream position x three clearly grouped non-zero levels of DoD is an indication that there are only two bottlenecks, i.e., the controlling constraints are only two: one responsible for a

Table 2
The matrix $\boldsymbol{a} = [a_{ij}]$ representing the main rate-controlling constraints as identified in [19].

i	Physical meaning of the constraint		O a_{i1}	O_2 a_{i2}	H a_{i3}	H_2 a_{i4}	OH a_{i5}	H_2O a_{i6}	HO_2 a_{i7}	H_2O_2 a_{i8}
EH	Total number of hydrogen nuclei	$\boldsymbol{a}_{\rm EH} = [$	0	0	1	2	1	2	1	2]
EO	Total number of oxygen nuclei	$\boldsymbol{a}_{\rm EO} = [$	1	2	0	0	1	1	2	2]
M	Total number of moles	$\boldsymbol{a}_{\rm M} = [$	1	1	1	1	1	1	1	1]
FV	Total free valence	$\boldsymbol{a}_{\rm FV} = [$	2	0	1	0	1	0	1	0]
FO	Total free oxygen	$\boldsymbol{a}_{\rm FO} = [$	1	0	0	0	1	1	0	0]
$H+H_2$	Used in Fig. 3	$\boldsymbol{a}_{\rm H+H_2} = [$	0	0	1	1	0	0	0	0]
$O+OH+H_2O$	Used in Fig. 3	$\boldsymbol{a}_{\rm O+OH+H_2O} = [$	1	0	0	0	1	1	0	0]

profile of DoD along the nozzle that is common to all reactions in "Group A": 7-8-9-10 and we may denote by $\mathrm{DoD}_A(x)$ (this turns out to be the M constraint), the other responsible for a DoD profile that is common to all reactions in "Group B": 12-15-16-17-19-22-24 and we denote by $\mathrm{DoD}_B(x)$ (this turns out to be identifiable with the FO − FV constraint). Reactions 1-2-3-4-5-6 instead form a third group that we call "group A + B" because it exhibits a DoD profile that is the sum of the preceding two, i.e., $\mathrm{DoD}_{A+B}(x) = \mathrm{DoD}_A(x) + \mathrm{DoD}_B(x)$. This clearly means that reactions in group A+B are effectively slowed down by both bottlenecks A and B.

The above observation is enough to identify the two corresponding constraints A and B. Indeed,

(1) reactions in Group 0 have no direct effect on either of the rates $\dot{c}_A$ and $\dot{c}_B$;
(2) reactions in Group A have no direct effect on the rate $\dot{c}_B$;
(3) reactions in Group B have no direct effect on the rate $\dot{c}_A$.

5. Basic logic of the new constraint identification methodology

From the observations in the previous section, the constraint matrix has four rows, with entries that we denote by a_{Aj}, a_{Bj}, $a_{{\rm EH}j}$, $a_{{\rm EO}j}$, the last two representing the elemental constraints (see Table 2). We can conclude that:

(1) the A row a_{Aj} of the constraint matrix a_{ij} is orthogonal to the fourteen columns of the stoichiometric matrix $\nu_{j\ell}$ with $\ell =$ 11-13-14-18-20-21-23 and 12-15-16-17-19-22-24, i.e., for all the reactions in Groups 0 and B,

$$\sum_{j=1}^{n_{sp}} a_{Aj}\nu_{j\ell}^{A} = 0 \tag{11}$$

(2) the B row a_{Bj} of the constraint matrix a_{ij} is orthogonal to the eleven columns of the stoichiometric matrix $\nu_{j\ell}$ with $\ell =$ 11-13-14-18-20-21-23 and 7-8-9-10, i.e., for all the reactions in Groups 0 and A,

$$\sum_{j=1}^{n_{sp}} a_{Bj}\nu_{j\ell}^{B} = 0 \tag{12}$$

(3) It is useful to remind that the EH row $a_{{\rm EH}j}$ and the EO row $a_{{\rm EO}j}$ of the constraint matrix $\boldsymbol{a} = [a_{ij}]$ are orthogonal to all the columns of the stoichiometric matrix $\boldsymbol{\nu} = [\nu_{j\ell}]$ for ℓ from 1 to n_r, i.e., for all the reactions in the DKM,

$$\sum_{j=1}^{n_{sp}} a_{{\rm EH}j}\nu_{j\ell} = 0 \text{ and } \sum_{j=1}^{n_{sp}} a_{{\rm EO}j}\nu_{j\ell} = 0 \tag{13}$$

As a consequence of Eqs. (13), once we have found vectors $\boldsymbol{a}_A = [a_{A1} \ \ldots \ a_{An_{\rm sp}}]$ and $\boldsymbol{a}_B = [a_{B1} \ \ldots \ a_{Bn_{\rm sp}}]$ that satisfy Eqs. (11) and (12), respectively, then we can substitute the linearly independent set of constraints $\boldsymbol{a}_{\rm EH}$, $\boldsymbol{a}_{\rm EO}$, $\boldsymbol{a}_A$, $\boldsymbol{a}_B$ with any other linearly independent set of vectors in their linear span.

From linear algebra, Eq. (11) means that vector $\boldsymbol{a}_A$ is in the left null space (co-kernel) of the 8 × 14 matrix $\boldsymbol{\nu_A} = [\nu_{j\ell} \ | \ell \in$ Groups 0 and B] and vector $\boldsymbol{a}_B$ in the left null space (co-kernel) of the 8 × 11 matrix $\boldsymbol{\nu_B} = [\nu_{j\ell} \ | \ell \in$ Groups 0 and A]. If we compute $\mathrm{coker}(\boldsymbol{\nu}_A) = \ker(\boldsymbol{\nu}_A^T)$ we find that it is three-dimensional (to compute the kernel, we use the MatLab function kA = null(A,'r') which applies the Gauss elimination algorithm to compute the basis of the kernel of matrix A, returned as the columns of matrix kA). In fact, $\mathrm{coker}(\boldsymbol{\nu}_A)$ is the linear span of the three linearly independent constraints $\boldsymbol{a}_{\rm EH}$, $\boldsymbol{a}_{\rm EO}$, and $\boldsymbol{a}_A$. However, we can easily identify directly the component of vector $\boldsymbol{a}_A$ that is orthogonal to the two-dimensional linear span of vectors $\boldsymbol{a}_{\rm EH}$ and $\boldsymbol{a}_{\rm EO}$, by computing instead the left null space of the 8 × 16 matrix

$$\boldsymbol{S}_A = \left[\boldsymbol{\nu}_A \ \boldsymbol{a}_{\rm EH}^T \ \boldsymbol{a}_{\rm EO}^T\right] \tag{14}$$

shown in Table 3 obtained by appending to matrix $\boldsymbol{\nu}_A$ the column vectors representing the elemental constraints. Table 3 shows the components of the single vector $\boldsymbol{k}_A$ which constitutes the basis of the one-dimensional $\mathrm{coker}(\boldsymbol{S}_A)$. As noted in the table, $\boldsymbol{k}_A$ is a linear combination of the vectors $\boldsymbol{a}_{\rm EH}$, $\boldsymbol{a}_{\rm EO}$, and $\boldsymbol{a}_{\rm M}$, therefore, the non-elemental constraint identified by $\mathrm{coker}(\boldsymbol{S}_A)$ is essentially the 'total number of moles' constraint $\boldsymbol{a}_{\rm M}$.

Similarly, $\mathrm{coker}(\boldsymbol{\nu}_B)$ is the three-dimensional linear span of constraints $\boldsymbol{a}_{\rm EH}$, $\boldsymbol{a}_{\rm EO}$, and $\boldsymbol{a}_B$. So, to identify the component of vector $\boldsymbol{a}_B$ that is orthogonal to the two-dimensional linear span of constraints $\boldsymbol{a}_{\rm EH}$ and $\boldsymbol{a}_{\rm EO}$, we compute the left null space of the matrix

$$\boldsymbol{S}_B = \left[\boldsymbol{\nu}_B \ \boldsymbol{a}_{\rm EH}^T \ \boldsymbol{a}_{\rm EO}^T\right] \tag{15}$$

shown in Table 3 obtained by appending to matrix $\boldsymbol{\nu}_B$ the column vectors representing the elemental constraints. Table 3 shows also the components of the single vector $\boldsymbol{k}_B$ which constitutes the basis of the one-dimensional $\mathrm{coker}(\boldsymbol{S}_B)$. As noted in the table, $\boldsymbol{k}_B$ is a linear combination of the vectors $\boldsymbol{a}_{\rm EH}$, $\boldsymbol{a}_{\rm EO}$, and $\boldsymbol{a}_{\rm FO} - \boldsymbol{a}_{\rm FV}$, therefore, the non-elemental constraint identified by $\mathrm{coker}(\boldsymbol{S}_B)$ is essentially the 'difference between total free oxygen and total free valence' constraint $\boldsymbol{a}_{\rm FO} - \boldsymbol{a}_{\rm FV}$.

Finally, therefore, the main result of the new algorithm is that it identifies automatically the set of four constraints (EH, EO, M, FO − FV) as the one effectively governing the dynamics under the given geometry and boundary conditions. Importantly, it does so with no need for any additional physical insight, other than the inspection of the grouping of reactions that in Fig. 2 is quite evident.

To validate the method so far, Fig. 3 shows the results of an RCCE simulation using the 4-constraints set (EH, EO, M, FO − FV) compared with the results of the DKM simulation as well as the RCCE simulations based on the sets of constraints obtained in [19], namely, the 5-constraints set (EH, EO, M, FO, FV) and the 4-constraints set (EH, EO, $H+H_2$, $O+OH+H_2O$). The specific impulse $I_{\rm sp}$ is defined as the thrust force per unit mass flow rate of the propellant. Under the assumed isentropic expansion to back pressure throughout the nozzle, $I_{\rm sp}$ is equal to the flow velocity at the nozzle exit plane, $u_{\rm exit}$. In rocketry it is common to divide

Table 3
The matrices $\boldsymbol{S}_A$ and $\boldsymbol{S}_B$ whose co-kernels uniquely identify the two constraints effectively controlling the kinetics under the nozzle geometry and boundary conditions that generate the full DKM profiles of DoD shown in Fig. 2.

Matrix $\boldsymbol{S}_A$																coker($\boldsymbol{S}_A$)	$(\boldsymbol{a}_M)_j =$
11	13	14	18	20	21	23	12	15	16	17	19	22	24	EH	EO	$(\boldsymbol{k}_A)_j$	$(-\frac{1}{2}\boldsymbol{k}_A + \frac{3}{8}\boldsymbol{a}_{EH} + \frac{3}{8}\boldsymbol{a}_{EO})_j$
−1	−1	1	0	0	1	0	−1	1	0	0	0	0	0	1	0	−5/4	1
0	0	−1	0	0	0	0	1	0	1	0	0	1	1	2	0	−1/2	1
1	0	−1	−1	1	0	0	0	−1	−1	−1	−1	0	0	0	1	−5/4	1
−1	0	0	1	−1	0	0	0	0	1	0	0	0	0	0	2	−1/2	1
1	1	1	0	−1	−2	−1	1	0	0	2	1	−1	0	1	1	−1/2	1
0	0	0	0	1	1	1	0	1	0	0	1	1	0	1	2	1/4	1
0	1	0	1	0	0	1	−1	−1	−1	−1	0	−1	−2	2	1	1/4	1
0	−1	0	−1	0	0	−1	0	0	0	0	−1	0	1	2	2	1	1

Matrix $\boldsymbol{S}_B$													coker($\boldsymbol{S}_B$)	$(\boldsymbol{a}_{FO} - \boldsymbol{a}_{FV})_j =$
11	13	14	18	20	21	23	7	8	9	10	EH	EO	$(\boldsymbol{k}_B)_j$	$(-\frac{1}{6}\boldsymbol{k}_B - \frac{5}{24}\boldsymbol{a}_{EH} + \frac{1}{8}\boldsymbol{a}_{EO})_j$
−1	−1	1	0	0	1	0	0	0	0	0	1	0	−19/4	−1
0	0	−1	0	0	0	0	−1	−1	−1	0	2	0	5/2	0
1	0	−1	−1	1	0	0	−1	−1	−1	0	0	1	−27/4	−1
−1	0	0	1	−1	0	0	0	0	0	0	0	2	−3/2	0
1	1	1	0	−1	−2	−1	0	0	0	−2	1	1	1/2	0
0	0	0	0	1	1	1	0	0	0	0	1	2	23/4	1
0	1	0	1	0	0	1	1	1	1	0	2	1	−17/4	−1
0	−1	0	−1	0	0	−1	0	0	0	1	2	2	1	0

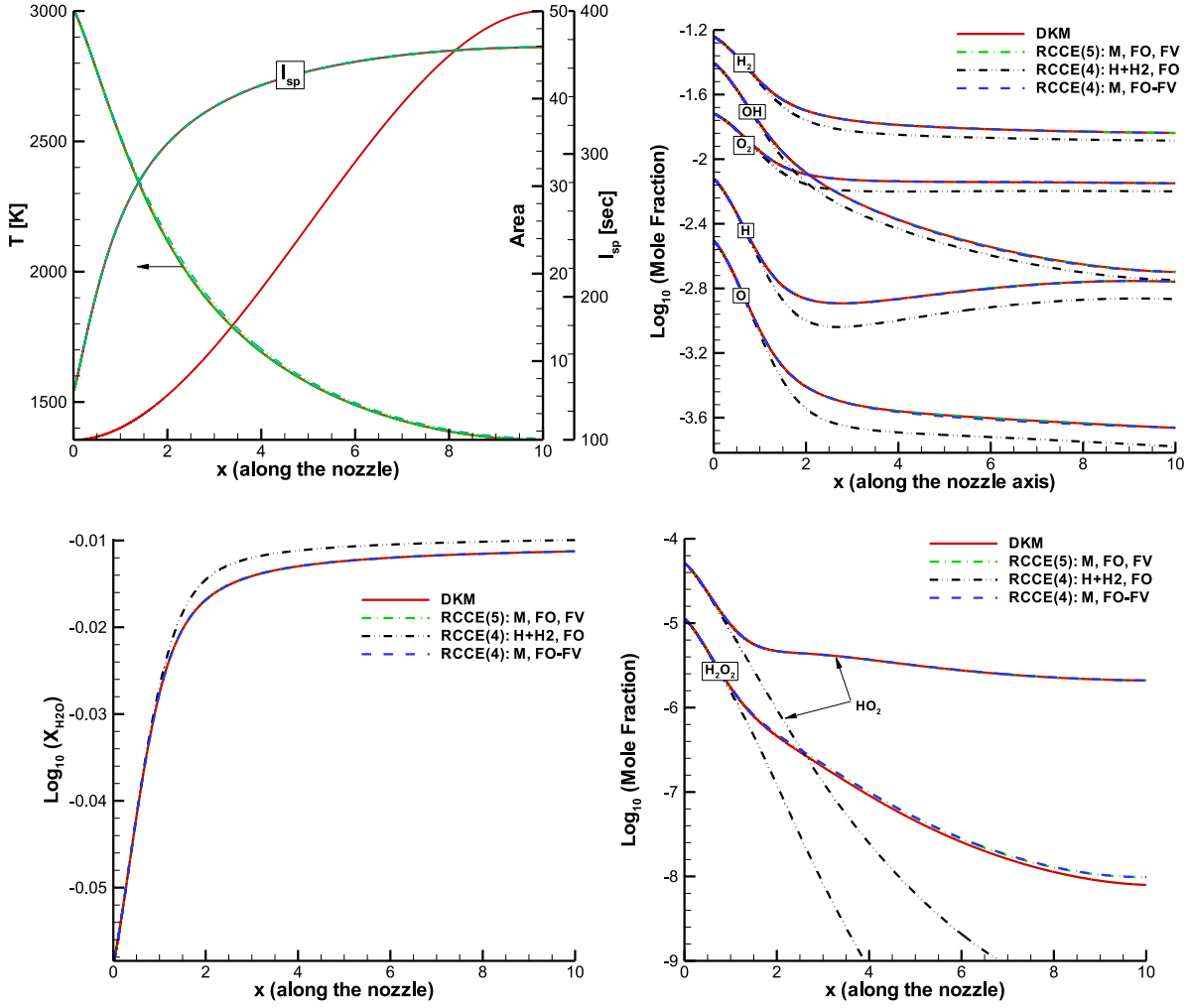

Fig. 3. Plots of temperature T, specific impulse I_{sp}, and mole fractions X_j of all species versus dimensionless downstream axial distance x resulting from RCCE simulations compared with the corresponding data from the underlying DKM simulation, for the same nozzle dimensionless area $A(x)$ and sonic throat inlet conditions as in [19]. The constraints used in the different RCCE simulations are: the two sets of constraints obtained in [19], namely, the 5-constraints set RCCE(5) = ($\boldsymbol{a}_{EH}$, $\boldsymbol{a}_{EO}$, $\boldsymbol{a}_M$, $\boldsymbol{a}_{FO}$, $\boldsymbol{a}_{FV}$) and the 4-constraints set RCCE(4) = ($\boldsymbol{a}_{EH}$, $\boldsymbol{a}_{EO}$, $\boldsymbol{a}_{H+H_2}$, $\boldsymbol{a}_{O+OH+H_2O}$); and the 4-constraints set resulting from the DoD analysis described in the present section, namely, RCCE(4) = ($\boldsymbol{a}_{EH}$, $\boldsymbol{a}_{EO}$, $\boldsymbol{a}_M$, $\boldsymbol{a}_{FO} - \boldsymbol{a}_{FV}$).

the specific impulse by the gravitational acceleration, g_0, to make it independent of the system of units. Therefore, here I_{sp} stands for u_{exit}/g_0, which has units of time.

In the following sections we provide an automatic algorithm also for grouping the reactions based on the analysis of DoD results from the DKM simulation. Indeed, it is possible to further systematize our new methodology for RCCE constraint selection for full automation also of the reaction grouping step, which so far we have achieved easily by inspection of Fig. 2, but in more general cases can be much less immediate, especially when more than 2 bottlenecks are in effect. Indeed, with two bottlenecks we have seen that the reactions essentially assemble into 4 basic groups (0, A, B, A + B) but in principle also other possible combinations like A + 2B and so on are possible. With three bottlenecks, reactions can form at least 8 basic groups (0, A, B, C, A + B, A + C, B + C, A + B + C) but again also higher integer and even fractional linear combinations are in principle possible. With four bottlenecks, the basic groups are 16 (0, A, B, C, D, A + B, A + C, A + D, B + C, B + D, C + D, A + B + C, A + B + D, A + C + D, B + C + D, A + B + C + D) plus other combinations. It is clear that the identification by simple inspection becomes very difficult, if not impossible, as the number of bottlenecks increases beyond three. However, we show below that this apparent complexity can be mathematically rationalized to obtain a fully automatable procedure for constraint selection given an acceptable value of a suitably defined degree of approximation.

6. General relations between DoDs and stoichiometric coefficients. Definition of the Overall DoD vector

In this section we discuss a number of preliminary observations and introduce the notation that in the next section is used to propose our new procedure for systematic constraint selection. The considerations in the present section are completely general, in the sense of independent of the assumptions of the RCCE method or of any other model reduction scheme; indeed, they are also independent of the assumption of ideal Gibbs-Dalton mixture of ideal gases that is typically adopted for the simple treatment of reacting gas mixtures.

We have already recalled in the previous section that the entropic chemical potentials $\lambda_j = -\mu_j/RT$ are functions of temperature T, pressure p, and composition vector $\boldsymbol{N} = [N_1 \ \dots \ N_{n_{sp}}]$, i.e.,

$$\lambda_j = \lambda_{j,\mathrm{off}}(T, p, \boldsymbol{N}) = -\frac{\mu_{j,\mathrm{off}}(T, p, \boldsymbol{N})}{RT} \tag{16}$$

Based on this relation, our first step is to transform the state representation from composition space $(T, p, \boldsymbol{N})$ to entropic chemical potentials space $(T, p, \boldsymbol{\Lambda})$

$$(T, p, \boldsymbol{N}) \leftrightarrow (T, p, \boldsymbol{\Lambda}) \tag{17}$$

where we introduce the vector

$$\boldsymbol{\Lambda} = \begin{bmatrix} \lambda_1 & \dots & \lambda_{n_{sp}} \end{bmatrix} \tag{18}$$

This alternative state representation is almost everywhere equivalent because the transformation (16) from $\boldsymbol{N}$ to $\boldsymbol{\Lambda}$ is almost everywhere invertible. Indeed, as shown for example in [34], the concavity of the fundamental relation $S_{\mathrm{off}}(U, V, \mathbf{N})$ of the surrogate system implies the convexity of the Gibbs free energy $G_{\mathrm{off}}(T, p, \mathbf{N})$ with respect to all the amounts N_j of constituents, therefore, $(\partial\lambda_j/\partial N_k)_{T,p,\mathbf{N}'} = (\partial^2 G_{\mathrm{off}}(T, p, \mathbf{N})/\partial N_j \partial N_k)_{T,p,\mathbf{N}'} > 0$ and the Jacobian determinant $|\partial(\lambda_1, \dots, \lambda_{n_{sp}})/\partial(N_1, \dots, N_{n_{sp}})|$ is strictly positive. The transformation is not invertible when some of the chemical potentials are infinite, like when, for ideal gas mixtures, some of the N_j's are zero, a case that we exclude from our treatment, meaning that for all practical purposes, when an N_j is initially zero, we substitute the zero with a very small value, like 10^{-30} mol.

Now, we observe that Eq. (6),

$$\phi_\ell = \sum_{j=1}^{n_{sp}} \lambda_j \nu_{j\ell} = \langle \boldsymbol{\Lambda} | \boldsymbol{\nu}_\ell \rangle \tag{19}$$

means that the DoD of any reaction ℓ is obtained by taking the scalar product of the vector $\boldsymbol{\Lambda}$ with the vector $\boldsymbol{\nu}_\ell = [\nu_{1\ell} \ \dots \ \nu_{n_{sp}\ell}]$ whose entries correspond to the ℓ-th column of the matrix $\boldsymbol{\nu}$ of stoichiometric coefficients.

In general the reactions in a given DKM are not all independent. In our example, the matrix $\boldsymbol{\nu}$ of stoichiometric coefficients is 8×24 and by virtue of the two elemental constraints (Relations (13)) its rank is $r = n_{sp} - n_{el} = 6$. A set of r independent reactions can be easily found by computing the reduced row echelon form of matrix $\boldsymbol{\nu}$, that we denote by $\mathrm{rref}(\boldsymbol{\nu})$. The ℓ's of the leading columns of $\mathrm{rref}(\boldsymbol{\nu})$ point to a set of independent reactions. For our example, computing $\mathrm{rref}(\boldsymbol{\nu})$ for the matrix $\boldsymbol{\nu}$ defined in Table 1, we find that reactions 1-2-3-6-7-10 form a linearly independent set. Note that the same procedure may yield a different linearly independent set if the reactions in the DKM are sorted in a different order.

Let us denote by $\mathrm{span}(\{\boldsymbol{\nu}_\ell\})$ the r-dimensional column space of the stoichiometric matrix $\boldsymbol{\nu}$, i.e., the linear span of the set of stoichiometric vectors $\boldsymbol{\nu}_\ell = [\nu_{1\ell} \ \dots \ \nu_{n_{sp}\ell}]$ whose entries are given by its columns, and by $\mathrm{coker}(\boldsymbol{\nu})$ the n_{el}-dimensional left null space of $\boldsymbol{\nu}$ spanned by the elemental constraint vectors $\{\boldsymbol{a}_{\mathrm{EL}_i}\}$ for $i = 1, \dots, n_{el}$. These two spaces, often called the *reactive subspace* and the *inhert subspace*, respectively, are orthogonal complements in the n_{sp}-dimensional real vector space $\mathbb{R}^n$, i.e., we may write

$$\mathbb{R}^n = \mathrm{span}(\{\boldsymbol{\nu}_\ell\}) \oplus \mathrm{coker}(\boldsymbol{\nu}) \tag{20}$$

meaning that any vector $\boldsymbol{x} = [x_1 \ \dots \ x_n]$ in $\mathbb{R}^n$ may be decomposed as $\boldsymbol{x} = \boldsymbol{x}_{\mathrm{span}(\{\boldsymbol{\nu}_\ell\})} + \boldsymbol{x}_{\mathrm{coker}(\boldsymbol{\nu})}$ with $\boldsymbol{x}_{\mathrm{span}(\{\boldsymbol{\nu}_\ell\})}$ in $\mathrm{span}(\{\boldsymbol{\nu}_\ell\})$, $\boldsymbol{x}_{\mathrm{coker}(\boldsymbol{\nu})}$ in $\mathrm{span}(\{\boldsymbol{\nu}_\ell\})$, and of course $\langle \boldsymbol{x}_{\mathrm{span}(\{\boldsymbol{\nu}_\ell\})} | \boldsymbol{x}_{\mathrm{coker}(\boldsymbol{\nu})} \rangle = 0$. Therefore, applying such decomposition to the vector $\boldsymbol{\Lambda}$ we may write

$$\boldsymbol{\Lambda} = \boldsymbol{\Lambda}_{\mathrm{DoD}} + \boldsymbol{\Lambda}_{\perp} \tag{21}$$

where for shorthand we introduced the notation

$$\boldsymbol{\Lambda}_{\mathrm{DoD}} = \boldsymbol{\Lambda}_{\mathrm{span}(\{\boldsymbol{\nu}_\ell\})} \text{ and } \boldsymbol{\Lambda}_{\perp} = \boldsymbol{\Lambda}_{\mathrm{coker}(\boldsymbol{\nu})} \tag{22}$$

We call $\boldsymbol{\Lambda}_{\mathrm{DoD}}$ the Overall Degree of Disequilibrium vector (ODoD). Clearly, we can rewrite Eq. (19) as follows:

$$\phi_\ell = \sum_{j=1}^{n_{sp}} \lambda_j \nu_{j\ell} = \langle \boldsymbol{\Lambda}_{\mathrm{DoD}} | \boldsymbol{\nu}_\ell \rangle \tag{23}$$

and, importantly, we can write

$$\boldsymbol{\Lambda}_{\mathrm{DoD}} = \sum_{k=1}^{r} \alpha_k \boldsymbol{\nu}_{\ell_k} \tag{24}$$

where the vectors $\{\boldsymbol{\nu}_{\ell_k}\}$ form a (non orthogonal) r-dimensional basis for $\mathrm{span}(\{\boldsymbol{\nu}_\ell\})$ constructed by choosing a subset of r linearly independent columns of the stoichiometric matrix identified by the column numbers ℓ_k, for $k = 1, \dots, r$ (in our example above, the six columns 1, 2, 3, 6, 7, 10 form such an independent set). It is also worth noting that the component $\boldsymbol{\Lambda}_{\perp}$ lies in the n_{el}-dimensional linear span of the elemental constraints (in our example, $n_{el} = 2$ and $\boldsymbol{\Lambda}_{\perp} = \gamma_{\mathrm{EH}}\boldsymbol{a}_{\mathrm{EH}} + \gamma_{\mathrm{EO}}\boldsymbol{a}_{\mathrm{EO}}$) and it is all that remains of vector $\boldsymbol{\Lambda}$ when complete chemical equilibrium is reached, because then (and

Table 4
Vectors $\boldsymbol{\nu}_{\ell_k}$ and the corresponding vectors $\boldsymbol{\chi}_k$ together with matrices $\boldsymbol{M}$ and $\boldsymbol{W}$ obtained with the procedure outlined in the text starting from the matrix $\boldsymbol{\nu}$ of stoichiometric coefficients given in Table 1.

$k=$	1	2	3	4	5	6	$k=$	1	2	3	4	5	6
$\ell_k=$	1	2	3	6	7	10							
j	$\nu_{j\ell_1}$	$\nu_{j\ell_2}$	$\nu_{j\ell_3}$	$\nu_{j\ell_4}$	$\nu_{j\ell_5}$	$\nu_{j\ell_6}$	Species	144 χ_{j1}	144 χ_{j2}	144 χ_{j3}	144 χ_{j4}	144 χ_{j5}	144 χ_{j6}
1	−2	−1	0	0	0	0	O	−51	−27	18	3	−21	−12
2	1	0	0	0	−1	0	O_2	42	−54	36	6	−42	−24
3	0	−1	−2	−1	−1	0	H	21	−51	−30	−21	3	−12
4	0	0	1	0	0	0	H_2	42	−102	84	−42	6	−24
5	0	1	0	−1	0	−2	OH	−30	66	−12	−18	−18	−24
6	0	0	0	1	0	0	H_2O	−9	15	−42	105	−15	−36
7	0	0	0	0	1	0	HO_2	63	−105	6	−15	105	−36
8	0	0	0	0	0	1	H_2O_2	−60	132	−24	−36	−36	96
$\boldsymbol{M}=$	5	2	0	0	−1	0	$144\boldsymbol{W}=$	105	−159	42	−9	63	−60
	2	3	2	0	1	−2		−159	345	−102	15	−105	132
	0	2	5	2	2	0		42	−102	84	−42	6	−24
	0	0	2	3	1	2		−9	15	−42	105	−15	−36
	−1	1	2	1	3	0		63	−105	6	−15	105	−36
	0	−2	0	2	0	5		−60	132	−24	−36	−36	96

only then) we have $\boldsymbol{\Lambda}_{\rm DoD}=0$, i.e., in general we can write

$$\boldsymbol{\Lambda}_{\perp}=\sum_{i=1}^{n_{\rm el}}\gamma_i^{\rm EL,DKM}\boldsymbol{a}_{{\rm EL}_i} \tag{25}$$

Substituting Eq. (24) into Eq. (23) for $\ell=\ell_{k'}$ we obtain

$$\phi_{k'}=\sum_{k=1}^{r}\alpha_k\langle\boldsymbol{\nu}_{\ell_k}|\boldsymbol{\nu}_{\ell_{k'}}\rangle \tag{26}$$

which can be viewed as a linear system of equations that we can solve for the α_k's because the $r\times r$ matrix $M_{kk'}=\langle\boldsymbol{\nu}_{\ell_k}|\boldsymbol{\nu}_{\ell_{k'}}\rangle$ is non-singular by virtue of the linear independence of the basis vectors $\boldsymbol{\nu}_{\ell_k}$. Hence, denoting its inverse by $\boldsymbol{W}=\boldsymbol{M}^{-1}$, we can write the solution of the system as

$$\alpha_k=\sum_{k'=1}^{r}\phi_{k'}W_{k'k} \tag{27}$$

Substituting into Eq. (24), we obtain $\boldsymbol{\Lambda}_{\rm DoD}=\sum_{k=1}^{r}\sum_{k'=1}^{r}\phi_{k'}W_{k'k}\boldsymbol{\nu}_{\ell_k}=\sum_{k=1}^{r}\phi_k\sum_{k'=1}^{r}W_{kk'}\boldsymbol{\nu}_{\ell_{k'}}$ which shows that we can transform to a more convenient (still non orthogonal) basis for span($\{\boldsymbol{\nu}_\ell\}$), defined by the transformation

$$\boldsymbol{\chi}_k=\sum_{k'=1}^{r}W_{kk'}\boldsymbol{\nu}_{\ell_{k'}} \tag{28}$$

with respect to which the coordinates of $\boldsymbol{\Lambda}_{\rm DoD}$ are the DoDs of the chosen r linearly independent reactions ℓ_k, for $k=1,\ldots,r$, i.e.,

$$\boldsymbol{\Lambda}_{\rm DoD}=\sum_{k=1}^{r}\phi_k\ \boldsymbol{\chi}_k \tag{29}$$

It is important to note that the basis vectors $\boldsymbol{\chi}_k$ can be computed once and for all for the given DKM by simple algebraic operations based exclusively on the matrix $\boldsymbol{\nu}$ of stoichiometric coefficients. Note again that the same procedure may yield different linearly independent sets of reactions and basis vectors $\boldsymbol{\chi}_k$ if the columns of the stoichiometric matrix are sorted in a different order. Table 4 shows for our example the vectors $\boldsymbol{\nu}_{\ell_k}$ and the corresponding vectors $\boldsymbol{\chi}_k$ together with matrices $\boldsymbol{M}$ and $\boldsymbol{W}$.

Relation (29) is very important for the algorithm of automatic selection of RCCE constraints we introduce in the next section. It is also important in general for the analysis of results obtained from a DKM simulation because it allows to construct the ODoD vector $\boldsymbol{\Lambda}_{\rm DoD}$ from the values ϕ_k of the DoDs of a subset of only r independent reactions. In a general unsteady and inhomogeneous set-up, the results of a DKM simulation will be functions of both position $\boldsymbol{x}$ and time t, therefore, Eq. (29) rewrites as

$$\boldsymbol{\Lambda}_{\rm DoD}(\boldsymbol{x},t)=\sum_{k=1}^{r}\phi_k(\boldsymbol{x},t)\ \boldsymbol{\chi}_k \tag{30}$$

In a homogeneous unsteady problem, such as the one typically considered for the prediction of ignition delay time of a gas mixture, this relation would reduce to

$$\boldsymbol{\Lambda}_{\rm DoD}(t)=\sum_{k=1}^{r}\phi_k(t)\ \boldsymbol{\chi}_k \tag{31}$$

In our steady-state quasi-one-dimensional nozzle example, it reduces to

$$\boldsymbol{\Lambda}_{\rm DoD}(x)=\sum_{k=1}^{r}\phi_k(x)\ \boldsymbol{\chi}_k \tag{32}$$

7. RCCE constraints are basis vectors for the approximate linear span of the ODoD vectors

As seen in the previous section, the number of vectors $\boldsymbol{\chi}_k$ in Eq. (30) is equal to the rank r of the matrix of stoichiometric coefficients of the DKM. Therefore, as the spatial and time coordinates $(\boldsymbol{x},t)$ span their respective ranges for the results of a given full DKM simulation, in general the ODoD vector $\boldsymbol{\Lambda}_{\rm DoD}(\boldsymbol{x},t)$, defines an $(\boldsymbol{x},t)$ family of vectors in the r-dimensional subspace spanned by the vectors $\boldsymbol{\chi}_k$. In a homogeneous unsteady problem and in a steady-state one-dimensional problem this is a one-parameter family.

As we recalled in the Introduction, the general physical idea behind the RCCE method is that in most particular problems and set of conditions, the non-equilibrium chemical dynamics is controlled by a number of bottleneck mechanisms that is generally smaller (often much smaller) than r. The bottlenecks are responsible for keeping the state far from equilibrium. This qualitative concept can now be quantified thanks to Eq. (30).

Before proceeding, it is worth noting that within the domain of validity of the ideal Gibbs-Dalton mixture model: (i) the chemical potentials may be written as $\mu_{j,\rm off}(T,p,\boldsymbol{N})=\mu_{jj}(T,p)+RT\ln(X_j)$ (recall that per our notation, the double subscript refers to the pure substance properties), where $X_j=N_j/N$ are the mole fractions and $N=\sum_j N_j$; (ii) the entropic chemical potentials (defined by $\lambda_j=-\mu_j/RT$) are $\lambda_{j,\rm off}(T,p,\boldsymbol{N})=\lambda_{jj}(T,p)-\ln(X_j)$; and (iii) we may write $\boldsymbol{\Lambda}=\boldsymbol{\Lambda}_{\rm pure}(T,p)-\ln(\boldsymbol{X})$ where, of course, $\ln(\boldsymbol{X})$ is shorthand notation for the vector with entries

$[\ln(X_1)\ \ldots\ \ln(X_{n_{sp}})]$ and $\mathbf{\Lambda}_{\rm pure}(T,p) = [\lambda_{11}(T,p)\ \ldots\ \lambda_{n_{sp}n_{sp}}(T,p)]$. Therefore, using Eq. (21), i.e., the orthogonal decomposition $\mathbf{\Lambda} = \mathbf{\Lambda}_{\rm DoD} + \mathbf{\Lambda}_\perp$, we may write

$$\mathbf{\Lambda}_{\rm DoD} = \mathbf{\Lambda}_{\rm pure}(T,p) - \mathbf{\Lambda}_\perp - \ln(\boldsymbol{X}) \tag{33}$$

from which it follows that for given T, p and $\mathbf{\Lambda}_\perp$, the ODoD vector $\mathbf{\Lambda}_{\rm DoD}$ is directly related to the logarithms of the mole fractions.

We also recall (e.g., from Ref. [12]) that in a RCCE state, the species mole fractions are given by

$$\frac{N_j}{N} = \exp\left(\lambda_{jj}(T,p) - \sum_{i=1}^{n_{\rm el}} \gamma_i^{\rm EL,RCCE} a_{{\rm EL}_i j} - \sum_{i=1}^{n_c<r} \gamma_i^{\rm RCCE} a_{ij}\right) \tag{34}$$

or, equivalently,

$$\mathbf{\Lambda}_{\rm DoD}^{\rm RCCE} = \mathbf{\Lambda}_{\rm pure}(T,p) - \mathbf{\Lambda}_\perp^{\rm RCCE} - \ln\left(\boldsymbol{X}^{\rm RCCE}\right) \tag{35}$$

where, as noted before, the decomposition (21) allows us to identify

$$\mathbf{\Lambda}_\perp^{\rm RCCE} = \sum_{i=1}^{n_{\rm el}} \gamma_i^{\rm EL,RCCE} \boldsymbol{a}_{{\rm EL}_i} \tag{36}$$

and

$$\mathbf{\Lambda}_{\rm DoD}^{\rm RCCE} = \sum_{i=1}^{n_c<r} \gamma_i^{\rm RCCE} \boldsymbol{a}_i \tag{37}$$

Combining the above relations we may also write

$$\mathbf{\Lambda}_{\rm DoD}^{\rm RCCE} - \mathbf{\Lambda}_{\rm DoD} = \ln\left(\boldsymbol{X}/\boldsymbol{X}^{\rm RCCE}\right) + \sum_{i=1}^{n_{\rm el}} \left(\gamma_i^{\rm EL,DKM} - \gamma_i^{\rm EL,RCCE}\right)\boldsymbol{a}_{{\rm EL}_i} \tag{38}$$

where of course $\ln(\boldsymbol{X}/\boldsymbol{X}^{\rm RCCE})$ is shorthand for the vector $[\ln(X_1/X_1^{\rm RCCE})\ \ldots\ \ln(X_{n_{sp}}/X_{n_{sp}}^{\rm RCCE})]$.

The following subsection can be skipped by the reader who also skipped Sections 3–5.

7.1. Continuation of the example of Sections 3–5

Let us first consider our example and the results obtained in Sections 3–5. There, we found two constraints, the vectors $\boldsymbol{k}_A$ and $\boldsymbol{k}_B$, that allow very effectively to reproduce the DoD results shown in Fig. 2. Indeed, using the notation just introduced, let us write

$$\mathbf{\Lambda}_{\rm DoD}(x) \approx \gamma_A(x)\ \boldsymbol{k}_A + \gamma_B(x)\ \boldsymbol{k}_B \tag{39}$$

and substitute this relation in Eq. (23) to obtain

$$\phi_\ell(x) \approx \gamma_A(x)\ \langle \boldsymbol{k}_A | \boldsymbol{\nu}_\ell \rangle + \gamma_B(x)\ \langle \boldsymbol{k}_B | \boldsymbol{\nu}_\ell \rangle \tag{40}$$

Now recall from (11) that vector $\boldsymbol{k}_A$ is orthogonal to the elemental constraints and to all the reactions in groups 0 and B, and from (12) that vector $\boldsymbol{k}_B$ is orthogonal to the elemental constraints and to all the reactions in groups 0 and A. We can also easily verify that $\langle \boldsymbol{k}_A | \boldsymbol{\nu}_\ell \rangle = 2$ for all reactions in groups A (7-8-9-10) and A+B (1-2-3-4-5-6) and $\langle \boldsymbol{k}_B | \boldsymbol{\nu}_\ell \rangle = 12$ for all reactions in groups B (12-15-16-17-19-22-24) and A+B (1-2-3-4-5-6). As a result, Eq. (40) yields

$$\begin{aligned}
\phi_{\ell\ \in\ \text{group 0}}(x) &\approx 0\\
\phi_{\ell\ \in\ \text{group A}}(x) &\approx 2\ \gamma_A(x)\\
\phi_{\ell\ \in\ \text{group B}}(x) &\approx 12\ \gamma_B(x)\\
\phi_{\ell\ \in\ \text{group A+B}}(x) &\approx 2\ \gamma_A(x) + 12\ \gamma_B(x)
\end{aligned} \tag{41}$$

and, therefore, if we take the function $2\ \gamma_A(x)$ to coincide with the average of the curves in Fig. 2 labelled 7-8-9-10 (group A) and the function $12\ \gamma_B(x)$ to coincide with the average of the curves labeled 12-15-16-17-19-22-24 (group B) we closely reproduce all the DoD results, including those for groups 0 and A+B. Eq. (39) shows that as the spatial coordinate x spans the length of the nozzle, the ODoD vector $\mathbf{\Lambda}_{\rm DoD}(x)$ remains approximately confined "within a small distance" from the 2-dimensional subspace spanned by the two constraint vectors $\boldsymbol{k}_A$ and $\boldsymbol{k}_B$.

We can actually rewrite Eq. (39) as follows:

$$\mathbf{\Lambda}_{\rm DoD}(x) = \gamma_A(x)\ \boldsymbol{k}_A + \gamma_B(x)\ \boldsymbol{k}_B - \boldsymbol{\epsilon}(x) \tag{42}$$

which defines the "distance" vector $\boldsymbol{\epsilon}(x)$. With $\gamma_A(x)$ and $\gamma_B(x)$ determined from the curves in Fig. 2 as just specified, we can estimate vector $\boldsymbol{\epsilon}(x)$. We find that $\langle \boldsymbol{\epsilon}(x) | \boldsymbol{k}_A \rangle = -1.14 \times 10^{-6}$ and $\langle \boldsymbol{\epsilon}(x) | \boldsymbol{k}_B \rangle = -2.15 \times 10^{-6}$, thus showing that $\boldsymbol{\epsilon}(x)$ remains indeed approximately orthogonal to span$(\boldsymbol{k}_A, \boldsymbol{k}_B)$, the linear span of the constraints, and is therefore a good measure of the distance of $\mathbf{\Lambda}_{\rm DoD}(x)$ from it. Moreover, we find that $\max_x |\boldsymbol{\epsilon}| / \max_x |\mathbf{\Lambda}_{\rm DoD}| = 0.011$, confirming and quantifying the assertion that the distance between $\mathbf{\Lambda}_{\rm DoD}(x)$ and span$(\boldsymbol{k}_A, \boldsymbol{k}_B)$ remains relatively small for all x's. Clearly, the norm of vector $\boldsymbol{\epsilon}(x)$ also represents a measure of the "error" or "level of approximation" in a model order reduction scheme such as RCCE where for every x the vector $\gamma_A(x)\ \boldsymbol{k}_A + \gamma_B(x)\ \boldsymbol{k}_B$ is taken as the approximate representation of the vector $\mathbf{\Lambda}_{\rm DoD}(x)$.

A further observation is noteworthy at this point on the results shown in Fig. 3. There, we see that for all relevant variables the curves labelled RCCE(5): M, FO, FV and RCCE(4): M, FO – FV are almost identical. In terms of the foregoing discussion, the 5-constraints results of Ref. [19] mean that the ODoD vector $\mathbf{\Lambda}_{\rm DoD}(x)$ remains for all x's very close to span$(\boldsymbol{k}_M, \boldsymbol{k}_{FO}, \boldsymbol{k}_{FV})$, while the present 4-constraints results mean that it also remains for all x's very close to span$(\boldsymbol{k}_M, \boldsymbol{k}_{FO-FV})$, which is a two-dimensional subspace of the three-dimensional span$(\boldsymbol{k}_M, \boldsymbol{k}_{FO}, \boldsymbol{k}_{FV})$. In other words, the actual number of bottlenecks effectively controlling the non-equilibrium kinetics is not three but only two.

Actually, more accurate 4-constraints results and even reasonably accurate 3-constraints results can be obtained using the systematic constraint-selection method that we outline in the remainder of the present section. This is apparent in Fig. 4 which shows, for the same DKM simulation as in Fig. 3, the curves RCCE(4):PresentMethod obtained with the four constraints (EH, EO, $\boldsymbol{a}_1^{\varepsilon=1.205}$, $\boldsymbol{a}_2^{\varepsilon=1.205}$) and RCCE(3):PresentMethod obtained with the three constraints (EH, EO, $\boldsymbol{a}_1^{\varepsilon=6.6}$) where the constraint vectors $\boldsymbol{a}_1^{\varepsilon=6.6}$, $\boldsymbol{a}_1^{\varepsilon=1.205}$, $\boldsymbol{a}_2^{\varepsilon=1.205}$ are given explicitly in Appendix A where our new method is implemented in a simple MatLab code. It is clear from Fig. 4 that assuming a single bottleneck for the given nozzle geometry and boundary conditions pushes the model order reduction a bit too far, in that it produces relatively poor approximations of the concentrations of HO_2 and H_2O_2, indicating that the ODoD vectors $\mathbf{\Lambda}_{\rm DoD}(x)$ effectively unfold in two directions, not just one.

7.2. General case

We are finally ready to conclude this section by introducing our new systematic method to identify a set of n_c constraints $\boldsymbol{a}_i$ such that a given ODoD vector $\mathbf{\Lambda}_{\rm DoD}(x)$ remains for all x's relatively close to their linear span$(\{\boldsymbol{a}_i\})$ in the sense that for a sufficiently small $\boldsymbol{\epsilon}(x)$ we can write

$$\mathbf{\Lambda}_{\rm DoD}(x) = \sum_{i=1}^{n_c<r} \gamma_i^{\rm RCCE}(x) \boldsymbol{a}_i - \boldsymbol{\epsilon}(x) \tag{43}$$

where the number n_c of constraints is smaller (preferably, much smaller) than the rank r of the matrix of stoichiometric coefficients.

In practical computations, the ODoD vector is usually in discretized form, $\mathbf{\Lambda}_{\rm DoD}(z_p)$, where z stands for either x or t or $(\boldsymbol{x}, t)$, depending on the problem, and the index p labels the P points of the discretization grid, where P is usually a large integer. The ODoD vector is thus represented by the $n_{sp} \times P$ matrix $\Lambda_{{\rm DoD},jp}$.

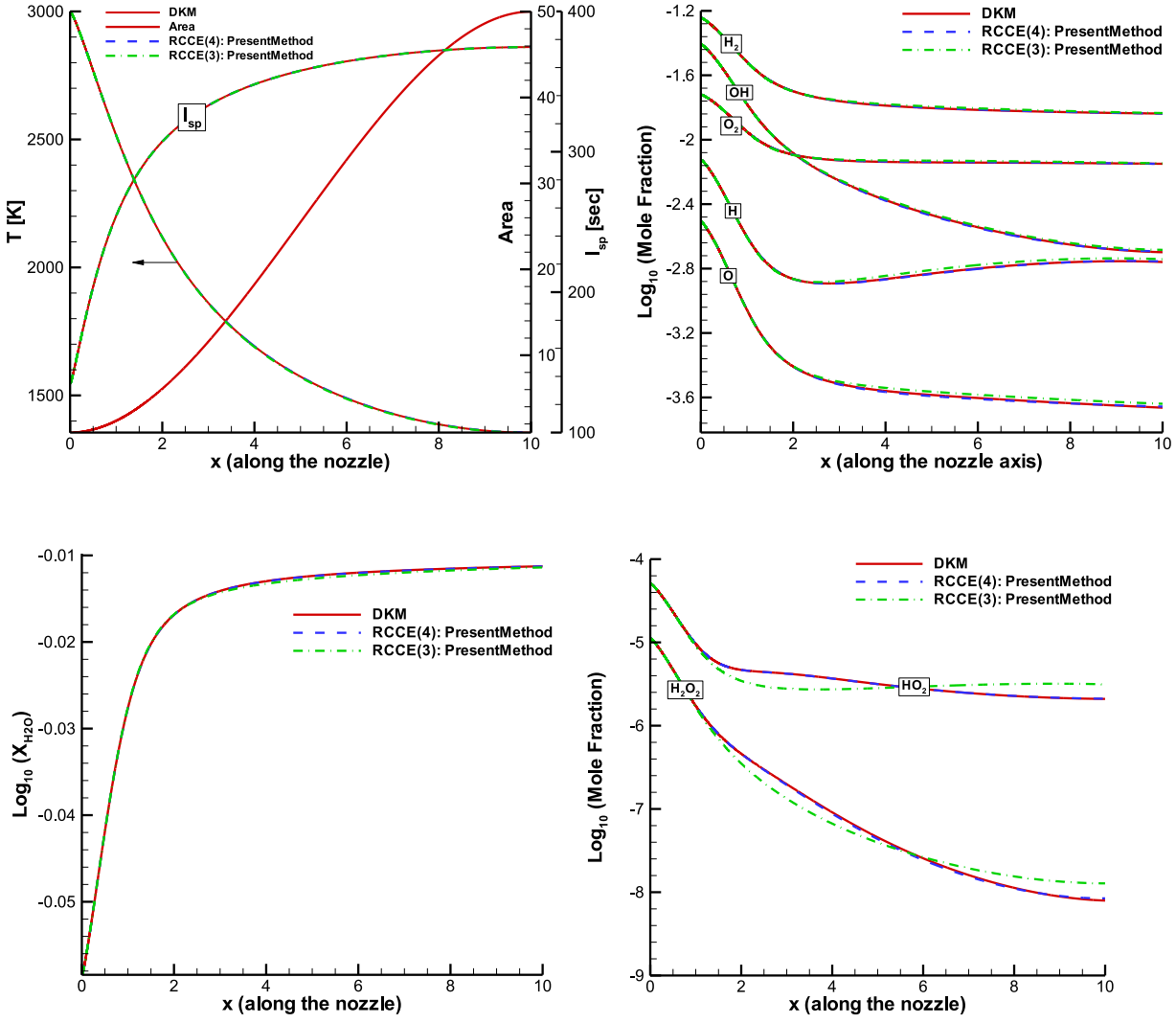

Fig. 4. Plots of temperature T, specific impulse I_{sp}, and mole fractions X_j of all species versus dimensionless downstream axial distance x resulting from RCCE simulations compared with the corresponding data from the underlying DKM simulation, for the conditions detailed in Fig. 1. Here we compare the results of RCCE simulations based on two sets of constraints selected using the ARREFADD method described in Section 7.2: the 4-constraints set RCCE(4): PresentMethod $=(\boldsymbol{a}_{\rm EH}, \boldsymbol{a}_{\rm EO}, \boldsymbol{a}_1^{\varepsilon=1.205}, \boldsymbol{a}_2^{\varepsilon=1.205})$; and the 3-constraints set RCCE(3): PresentMethod $=(\boldsymbol{a}_{\rm EH}, \boldsymbol{a}_{\rm EO}, \boldsymbol{a}_1^{\varepsilon=6.6})$ where $\boldsymbol{a}_1^{\varepsilon=6.6}$, $\boldsymbol{a}_1^{\varepsilon=1.205}$, $\boldsymbol{a}_2^{\varepsilon=1.205}$ are given explicitly in Appendix A together with the MatLab code used to compute them from the full DKM simulation.

We already know from Eq. (29) that this matrix has rank $r = n_{\rm sp} - n_{\rm el}$. However, we search for an approximate $\Lambda^{\rm RCCE}_{{\rm DoD},jp}$ of rank $n_{\rm c} < r$. From Eq. (43) it is clear that if all $\boldsymbol{\epsilon}(z_p)$ are negligible, then we can assume

$$\boldsymbol{\Lambda}_{\rm DoD}(z_p) \approx \boldsymbol{\Lambda}^{\rm RCCE}_{\rm DoD}(z_p) = \sum_{i=1}^{n_{\rm c}<r} \gamma_i^{\rm RCCE}(z_p)\boldsymbol{a}_i \tag{44}$$

so that the range of matrix $\Lambda^{\rm RCCE}_{{\rm DoD},jp}$ is in the linear span of the $n_{\rm c}$ column vectors $a_{j1}, \ldots, a_{jn_{\rm c}}$. If the constraint vectors $\boldsymbol{a}_i$ form an orthonormal set, $\langle \boldsymbol{a}_i | \boldsymbol{a}_k \rangle = \delta_{ik}$, then

$$\gamma_i^{\rm RCCE}(z_p) \approx \langle \boldsymbol{a}_i | \boldsymbol{\Lambda}_{\rm DoD}(z_p) \rangle \tag{45}$$

or, equivalently,

$$\boldsymbol{\Lambda}^{\rm RCCE}_{\rm DoD}(z_p) \approx \sum_{i=1}^{n_{\rm c}<r} \langle \boldsymbol{a}_i | \boldsymbol{\Lambda}_{\rm DoD}(z_p) \rangle \boldsymbol{a}_i \tag{46}$$

A set of constraint vectors $\boldsymbol{a}_i$ can be found by performing a Gauss-Jordan elimination procedure on the matrix $\Lambda_{{\rm DoD},jp}$ with a tolerance test that sets to zero the matrix elements that are below a prescribed threshold value ε. This standard linear-algebra procedure produces an approximate reduced row echelon form (RREF) of the matrix in which only the first $n_{\rm c}$ rows are non-zero, with $n_{\rm c}$ the smaller the higher we set the threshold value for the tolerance test, while $n_{\rm c} = r$ if the tolerance threshold is set to zero. Each tolerance threshold value ε determines a unique RREF matrix that we may denote as $\Lambda^{{\rm RREF}(\varepsilon)}_{{\rm DoD},jp}$. The positions of the pivots in the RREF matrix $\Lambda^{{\rm RREF}(\varepsilon)}_{{\rm DoD},jp}$, i.e., their column labels $p_1, \ldots, p_{n_{\rm c}}$, identify the $n_{\rm c}$ columns $\boldsymbol{\Lambda}^{{\rm RREF}(\varepsilon)}_{{\rm DoD},p_1}, \ldots, \boldsymbol{\Lambda}^{{\rm RREF}(\varepsilon)}_{{\rm DoD},p_{n_{\rm c}}}$ of the original matrix $\Lambda_{{\rm DoD},jp}$ that form a basis for its approximate range with respect to tolerance ε. Therefore, any orthonormal basis for the linear span of these column vectors, is the set of $n_{\rm c}$ RCCE constraint vectors $\boldsymbol{a}_i^{\varepsilon}$ that we are looking for, to be used in Eq. (46) and in our RCCE simulation together with the elemental constraints. This concludes the heart of our algorithm.

What remains to be chosen is the value of ε. The optimal choice of the largest acceptable value for ε for a given problem depends on the level of desired accuracy, and its discussion goes beyond the scope of the present paper, because in general it requires to analyse also the governing differential equations for the other variables

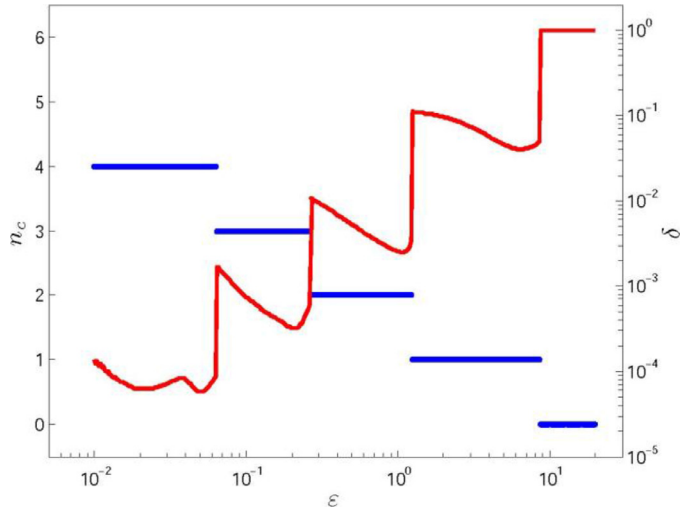

Fig. 5. Number of constraints $n_c(\varepsilon)$ (stepwise function, left axis) and the corresponding mean error $\delta(\varepsilon)$ (right axis), for various values of the tolerance threshold ε, obtained by applying the new systematic constraint selection procedure to the DoD data shown in Fig. 2, obtained from the full DKM simulation for the nozzle geometry shown in Fig. 1.

of the problem, such as velocity, temperature, pressure and other fields.

Here, instead, we simply note that we may repeat the above procedure for different values of the tolerance threshold ε, varying over some relevant range of values. As a result we find that $n_c(\varepsilon)$ is a stepwise decreasing function of ε, going from $n_c = r$ for sufficiently small ε (in which limit the RCCE model coincides with the full DKM), to $n_c = 0$ for sufficiently large ε (in which limit the RCCE model coincides with assuming complete chemical equilibrium). Figure 5 shows such stepwise behaviour for the sample DKM considered above and in Ref. [19], for values of ε in the range from 0.01 to 20, that result in $n_c(\varepsilon)$ from 4 to 0.

Figure 5 shows also the corresponding estimates of the mean error in terms of DoDs, defined as follows:

$$\delta(\varepsilon) = \frac{\text{mean}_{z_p}|\boldsymbol{\epsilon}^{\varepsilon}(z_p)|_2}{\text{mean}_{z_p}|\boldsymbol{\Lambda}_{\text{DoD}}(z_p)|_2} = \frac{\frac{1}{P}\sum_{p=1}^{P}\left(\sum_{j=1}^{n_{\text{sp}}}\left[\Lambda_{\text{DoD}j}(z_p) - \Lambda_{\text{DoD}j}^{\text{RCCE}(\varepsilon)}(z_p)\right]^2\right)^{1/2}}{\frac{1}{P}\sum_{p=1}^{P}\left(\sum_{j=1}^{n_{\text{sp}}}\left[\Lambda_{\text{DoD}j}(z_p)\right]^2\right)^{1/2}} \tag{47}$$

where mean_{z_p} represents the average value over the P grid points z_p (in our case, along the nozzle),

$$\boldsymbol{\Lambda}_{\text{DoD}}^{\text{RCCE}(\varepsilon)}(z_p) \approx \sum_{i=1}^{n_c(\varepsilon)<r} \langle \boldsymbol{a}_i^{\varepsilon}|\boldsymbol{\Lambda}_{\text{DoD}}(z_p)\rangle \boldsymbol{a}_i^{\varepsilon} \tag{48}$$

and, consistently with the definitions given above,

$$\boldsymbol{\epsilon}^{\varepsilon}(z_p) = \boldsymbol{\Lambda}_{\text{DoD}}^{\text{RCCE}(\varepsilon)}(z_p) - \boldsymbol{\Lambda}_{\text{DoD}}(z_p) \tag{49}$$

Notice that the vector norm $|\boldsymbol{\Lambda}_{\text{DoD}}(z_p)|_2$ represents an overall measure of Degree of Disequilibrium at grid point z_p, i.e, the distance of the actual DKM state at grid point z_p from complete equilibrium. For the data in Fig. 2, the average value along the nozzle downstream coordinate is $\text{mean}_{z_p}|\boldsymbol{\Lambda}_{\text{DoD}}(z_p)|_2 = 1.568$, whereas the maximum value is at the nozzle exit, $|\boldsymbol{\Lambda}_{\text{DoD}}(z_p)|_2 = 13.41$. Instead, $|\boldsymbol{\epsilon}^{\varepsilon}(z_p)|_2$ represents an overall measure of distance of the actual DKM state at grid point z_p from the $n_c(\varepsilon)$-dimensional constrained-equilibrium state manifold assumed as the state space in the RCCE reduced description.

From Fig. 5, we see that for values of ε such that $n_c(\varepsilon) = 0$, $\boldsymbol{\Lambda}_{\text{DoD}}^{\text{RCCE}(\varepsilon)}(z_p) = 0$ for all z_p's and, therefore, $\delta(\varepsilon) = 1$, i.e., the mean error is 100%, $\text{mean}_{z_p}|\boldsymbol{\epsilon}^{\varepsilon}(z_p)|_2 = \text{mean}_{z_p}|\boldsymbol{\Lambda}_{\text{DoD}}(z_p)|_2 = 1.568$, corresponding to the most drastic level of approximation (assumption of local complete chemical equilibrium) whereby the degrees of disequilibrium shown in Fig. 2 are essentially considered negligible.

With $n_c(\varepsilon) = 1$, i.e., a single constraint in addition to the elemental ones, Fig. 5 shows that the lowest mean error is 4.06% and obtains for a value of $\varepsilon = 6.499$. With $n_c(\varepsilon) = 2$, i.e., two constraints in addition to the elemental ones, the lowest mean error is 0.25% and obtains for $\varepsilon = 1.064$. With $n_c(\varepsilon) = 3$, the lowest mean error is 0.032% and obtains for $\varepsilon = 0.2107$. With $n_c(\varepsilon) = 4$, the lowest mean error is 0.006% and obtains for $\varepsilon = 0.0505$.

8. ASVDADD variant of the ARREFADD algorithm

The Eckart–Young theorem of linear algebra (see, e.g., Ref. [35] and references therein) provides a powerful tool to select optimal RCCE constraints, according to the ARREFADD method, if we accept a measure of the mean error δ to be minimized based on the Frobenius norm of the difference between the two $n_{\text{sp}} \times P$ matrices $\boldsymbol{\Lambda}_{\text{DoD}}(z_p)$ and $\boldsymbol{\Lambda}_{\text{DoD}}^{\text{RCCE}(n_c)}(z_p)$,

$$\delta_{\text{Fro}}^2(n_c) = \frac{\|\boldsymbol{\Lambda}_{\text{DoD}}(z_p) - \boldsymbol{\Lambda}_{\text{DoD}}^{\text{RCCE}(n_c)}(z_p)\|_{\text{Fro}}^2}{\|\boldsymbol{\Lambda}_{\text{DoD}}(z_p)\|_{\text{Fro}}^2} = \frac{\sum_{j=1}^{n_{\text{sp}}}\sum_{p=1}^{P}\left[\Lambda_{\text{DoD}j}(z_p) - \Lambda_{\text{DoD}j}^{\text{RCCE}(n_c)}(z_p)\right]^2}{\sum_{j=1}^{n_{\text{sp}}}\sum_{p=1}^{P}\left[\Lambda_{\text{DoD}j}(z_p)\right]^2} \tag{50}$$

Consider the singular value decomposition (SVD) [36] of the given $n_{\text{sp}} \times P$ matrix $\boldsymbol{\Lambda}_{\text{DoD}}(z_p)$

$$\boldsymbol{\Lambda}_{\text{DoD}}(z_p) = \boldsymbol{U}\boldsymbol{\Sigma}\boldsymbol{V}^{\boldsymbol{T}} \tag{51}$$

The $r = n_{\text{sp}} - n_{\text{el}}$ nonzero singular values σ_j are in decreasing order in the $n_{\text{sp}} \times P$ diagonal matrix $\boldsymbol{\Sigma}$ followed by the zero ones. The first r columns of the $n_{\text{sp}} \times n_{\text{sp}}$ orthogonal matrix $\boldsymbol{U}$ identify an orthonormal basis for the r-dimensional co-kernel of $\boldsymbol{\Lambda}_{\text{DoD}}(z_p)$. For a chosen number $n_c < r$ of constraints, let us define the $n_{\text{sp}} \times P$ diagonal matrix $\boldsymbol{\Sigma}^{\text{RCCE}(n_c)}$ obtained from $\boldsymbol{\Sigma}$ by setting to zero its diagonal elements with index $j > n_c$. By the Eckart–Young theorem, the $n_{\text{sp}} \times P$ matrix

$$\boldsymbol{\Lambda}_{\text{DoD}}^{\text{RCCE}(n_c)}(z_p) = \boldsymbol{U}\boldsymbol{\Sigma}^{\text{RCCE}(n_c)}\boldsymbol{V}^{\boldsymbol{T}} \tag{52}$$

represents the 'best approximation' to $\boldsymbol{\Lambda}_{\text{DoD}}(z_p)$ that can be achieved by a matrix of rank n_c, in the sense of minimizing the Frobenius measure δ_{Fro} of the approximation defined by Eq. (50), which turns out to be equal to the ratio

$$\delta_{\text{Fro}}(n_c) = \frac{\sum_{i=n_c+1}^{r}\sigma_i}{\sum_{i=1}^{r}\sigma_i} \tag{53}$$

where σ_{n_c+1} is the first neglected singular value. It follows that the first n_c columns of the matrix $\boldsymbol{U}$ identify an orthonormal basis for the n_c-dimensional co-kernel of $\boldsymbol{\Lambda}_{\text{DoD}}^{\text{RCCE}(n_c)}(z_p)$ and can be taken as the desired n_c 'best' RCCE constraints (in addition to the n_{el} elemental ones).

Considering that the first singular value, σ_1, is equal to the matrix norm $\|\boldsymbol{\Lambda}_{\text{DoD}}(z_p)\|_2$, and similarly $\sigma_{n_c+1} = \|\boldsymbol{\Lambda}_{\text{DoD}}(z_p) - \boldsymbol{\Lambda}_{\text{DoD}}^{\text{RCCE}(n_c)}(z_p)\|_2$, we may immediately compute also the error with respect to this norm, $\delta_2(n_c) = \sigma_{n_c+1}/\sigma_1$.

We call this variant of the ARREFADD algorithm ASVDADD, because it substitutes the RREF procedure with the SVD. This variant reduces the problem of minimizing the Frobenius or the matrix norm of $\boldsymbol{\epsilon}(x_p)$ for P samples x_p, to a standard problem in Principal Component Analysis (PCA) [37]. The great advantage of the ASVDADD procedure is that – at the expense of a specific but very natural choice for the measure of 'approximation' and hence

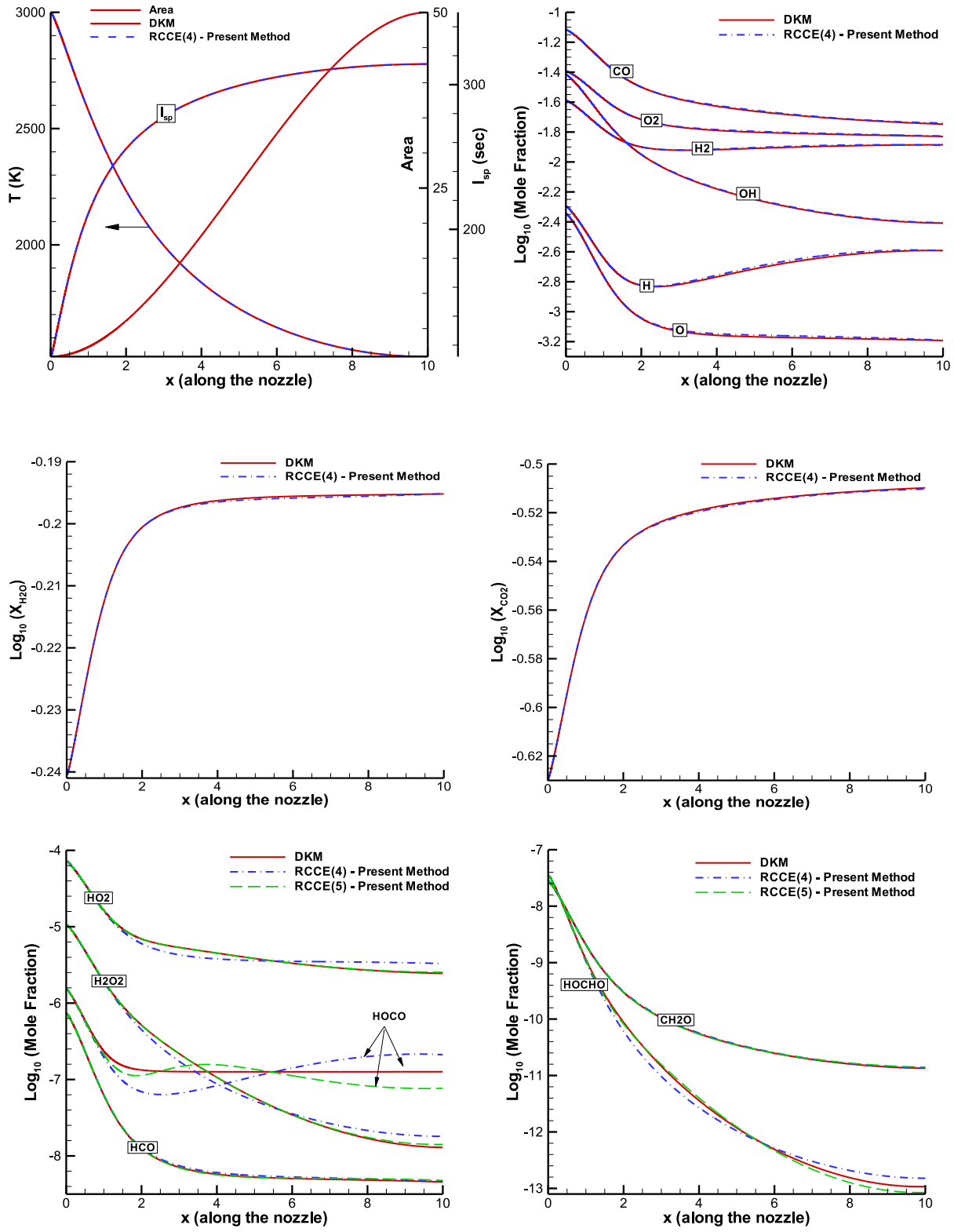

Fig. 6. Plots of temperature T, specific impulse I_{sp}, and mole fractions X_j of the main species versus dimensionless downstream axial distance x resulting from RCCE simulations compared with the corresponding data from the underlying DKM simulation, for the conditions detailed in Fig. 1. Here the comparisons are for the expansion/relaxation of the products of methane oxycombustion, between the results of a 29 species/133 reactions DKM simulation and two RCCE simulations with 4 and 5 total constraints. Constraints additional to the three elemental ones are obtained from the ARREFADD algorithm.

of 'optimality' of the choice of constraints – the SVD of $\mathbf{\Lambda}_{\rm DoD}(z_p)$ provides at once the entire spectrum of optimal constraints (the first r columns of $\boldsymbol{U}$) in decreasing order of importance and the corresponding Frobenius measure of the approximation involved in adopting a reduced RCCE description that considers only the first $n_{\rm c}$ columns of $\boldsymbol{U}$ as constraints. The optimal constraint vectors $\boldsymbol{a}_i$ are just the first $n_{\rm c}$ left-singular vectors of the $n_{\rm sp}\times P$ matrix formed from the P samples of $\mathbf{\Lambda}_{\rm DoD}$.

9. Validation for more complex cases

In this section we apply the proposed methodology to the following problems in the order of increasing complexity:

(1) the supersonic nozzle expansion/relaxation of the products of methane oxycombustion, with the same inlet conditions and nozzle geometry of the example considered so far;
(2) the supersonic nozzle expansion/relaxation of the products of hydrogen oxycombustion, with the same inlet conditions but a much shorter nozzle geometry producing a much more rapid expansion;
(3) the supersonic nozzle expansion/relaxation of the products of methane oxycombustion, with the same inlet conditions and much shorter nozzle geometry as in the previous case;
(4) ignition in a constant area plug flow reactor of a methane/oxygen mixture.

The results demonstrate the versatility, effectiveness, and robustness of the proposed method.

Figure 6 demonstrates the validity of the ARREFADD algorithm for the case of supersonic relaxation in a nozzle of identical geometry and with the same inlet conditions as for the results of Fig. 4, but for the combustion products of a methane/oxygen mixture modelled via a C1/H/O sub-mechanism of the GRI3 scheme [11]. The mechanism involves 29 species and 133 reactions. For this case, Fig. 6 shows a remarkable agreement between the DKM simulation and the RCCE simulation based only on a single kinetic constraint, in additional to the three obvious elemental constraints. Essentially, the complexity of this case turns out to be only mild, as the nonequilibrium dynamics is rate-controlled by a single bottleneck mechanism.

Next, we return to the hydrogen oxycombustion example studied in the previous sections and in Ref. [19], but with a nozzle length 100 times shorter. Figure 7 shows the DoD plots of the 24 reactions in the DKM obtained from a fully detailed DKM simulation. It is clear that the more rapid expansion results in the building up of a sizable Degree of Disequilibrium for almost all the reactions. Grouping the reactions by inspection like we have done in Sections 4 and 5 for the much simpler DoD plots in Fig. 2 is very difficult for the plots in Fig. 7 and would require a long set of trials and errors. Instead, the systematic method introduced in Sections 6 and 7 yields an automatic selection with identical ease of analysis. In this case, $\text{mean}_{z_p}|\mathbf{\Lambda}_{\rm DoD}(z_p)| = 6.638$,

Figure 8 shows the stepwise function $n_{\rm c}(\varepsilon)$ and the corresponding mean errors $\delta(\varepsilon)$. With $n_{\rm c}(\varepsilon) = 1,\ 2,\ 3,\ 4$, respectively, i.e., one, two, three, four constraints in addition to the elemental ones, the lowest mean errors are 3.98%, 0.807%, 0.106%, 0.0338% and obtain for $\varepsilon = 9.989,\ 2.142,\ 0.7003,\ 0.2289$.

Figure 9 shows the results of RCCE simulations compared with the underlying full DKM results. Clearly, the accuracy that is reached in this case assuming only one or two rate-controlling constraints (in addition to the elemental ones) is less than for the case shown in Fig. 4. However, the results are very reasonable considering the higher complexity of the nonequilibrium kinetics due to the much faster expansion, witnessed by the complex DoD plots in Fig. 7. A much higher accuracy would be clearly obtained by using the optimal (mean error 0.106%) 5-constraints set given in

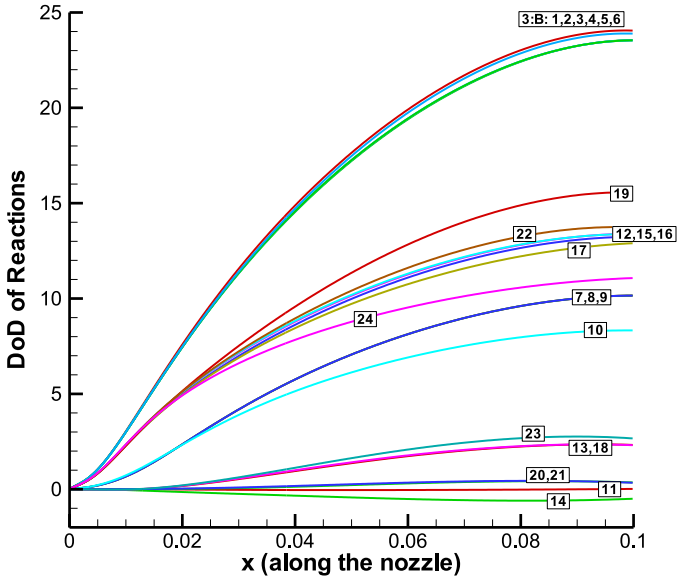

Fig. 7. Degrees of disequilibrium, $\phi_\ell = \ln(r_\ell^+/r_\ell^-)$, of the 24 reactions of the DKM in Table 1 plotted versus the dimensionless downstream coordinate x along the nozzle axis. The conditions are those detailed in Fig. 1 except for the nozzle length which here is 100 times shorter, resulting in DKM-DoD plots that exhibit more complexity than those in Fig. 2.

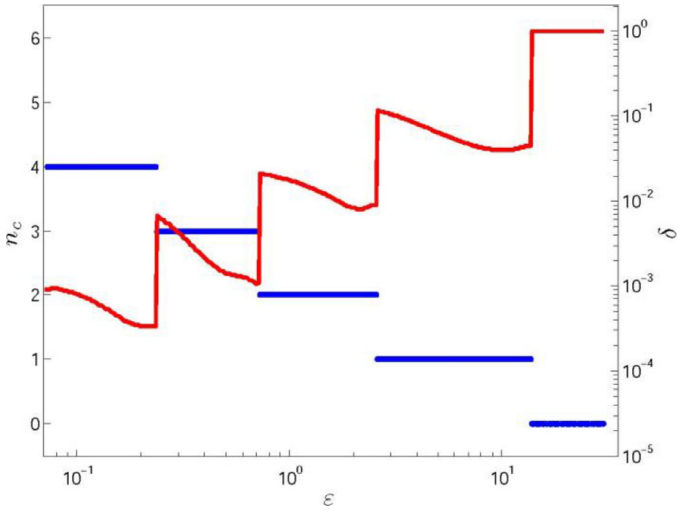

Fig. 8. Number of constraints $n_{\rm c}(\varepsilon)$ (stepwise function, left axis) and the corresponding mean error $\delta(\varepsilon)$ (right axis), for various values of the tolerance threshold ε, obtained by applying the new systematic constraint selection procedure to the DoD data shown in Fig. 7, obtained from the full DKM simulation.

Appendix B (plots not shown in Fig. 9 in the interest of readability).

When for the same rapid-expansion nozzle geometry of Fig. 9 we consider the combustion products of a methane/oxygen mixture, again modelled via the 29 species/133 reactions DKM scheme developed in [11] we obtain the results shown in Fig. 10 which shows that the RCCE(6) results approximate quite accurately the DKM results, meaning that under such conditions the nonequilibrium kinetics is essentially rate-controlled by only three bottleneck mechanisms.

Finally, Figs. 11 and 12 present the results for an ignition-delay type calculation, in which an additional level of complexity is introduced by the highly nonequilibrium inlet composition. We consider a constant-area plug-flow reactor with an unburnt

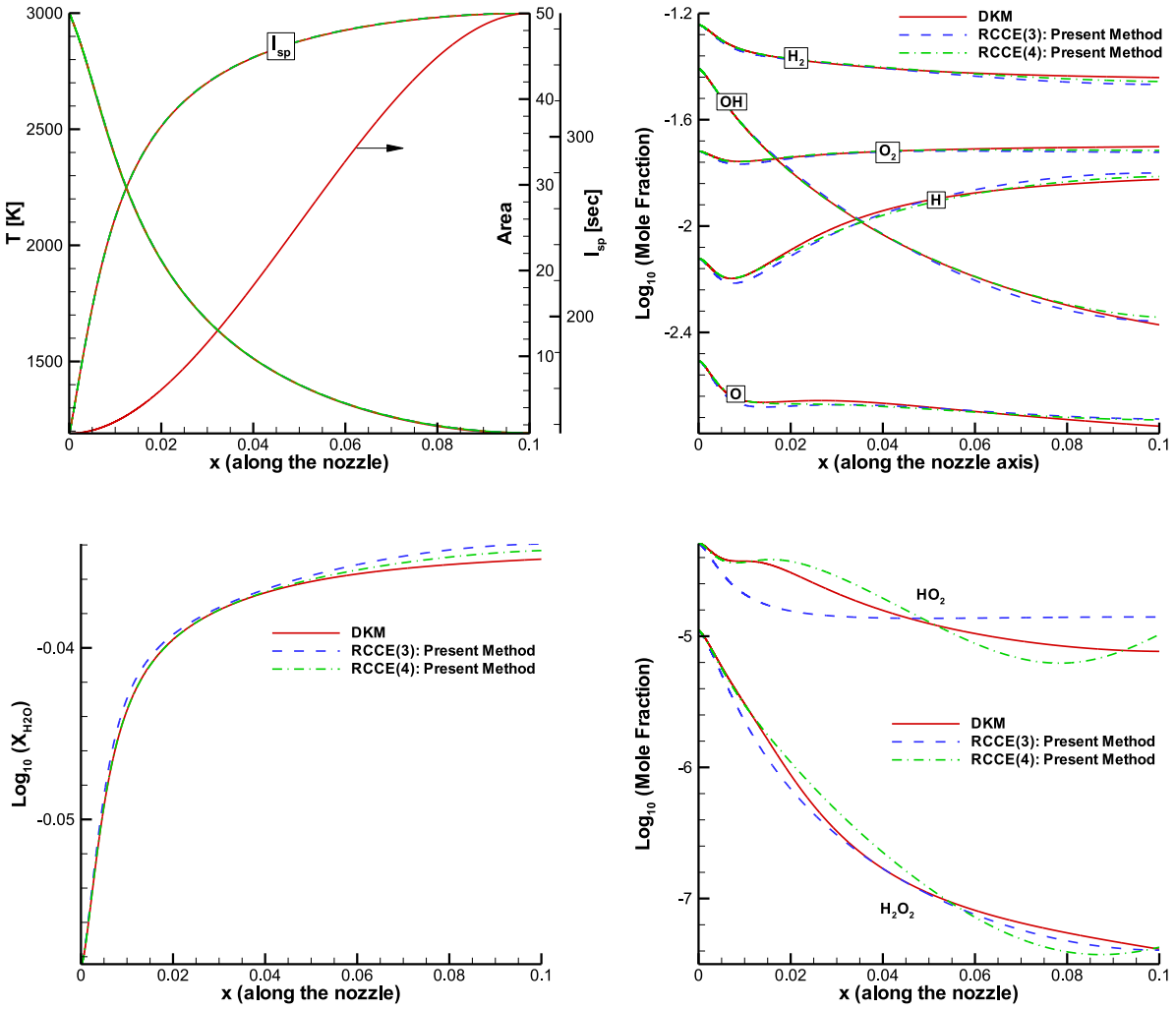

Fig. 9. Plots of temperature T, specific impulse I_{sp}, and mole fractions X_j of all species versus dimensionless downstream axial distance x resulting from RCCE simulations compared with the corresponding data from the underlying DKM simulation, for the conditions detailed in Fig. 1 except for the nozzle length which here is 100 times shorter. We compare the results of RCCE simulations based on two sets of constraints selected using our new systematic method: the 4-constraints set RCCE(4): PresentMethod $=(\boldsymbol{a}_{\rm EH}, \boldsymbol{a}_{\rm EO}, \boldsymbol{a}_1^2, \boldsymbol{a}_2^2)$; and the 3-constraints set RCCE(3): PresentMethod $=(\boldsymbol{a}_{\rm EH}, \boldsymbol{a}_{\rm EO}, \boldsymbol{a}_1^1)$ where $\boldsymbol{a}_1^1$, $\boldsymbol{a}_1^2$, $\boldsymbol{a}_2^2$ are given explicitly in Appendix A together with the MatLab code used to compute them from the results of a full DKM simulation.

methane/oxygen stoichiometric mixture at inlet with flow velocity small enough (Ma = 0.0001) that the flow remains subsonic in the entire channel from which it exits in complete chemical equilibrium. We consider two sets of inlet conditions: $p_0 = 10$ bar and $T_0 = 900$ K in Fig. 11; and $p_0 = 1$ bar and $T_0 = 1500$ K in Fig. 12. In Figs. 11 and 12 the constraints have been obtained for simplicity using the ASVDADD method. The higher complexity of the kinetics in these cases emerges from the difficulty to obtain a good approximation of the entire ignition delay process with a single set of constraints. In these two examples it is achieved with a relatively large number of ASVDADD constraints additional to the three elemental ones: thirteen for the conditions of Fig. 11 and ten for those of Fig. 12. Nevertheless, the plots show the robustness of the constraint selection methodology in the sense that as the number of constraints is increased the approximation essentially keeps improving, except for some fine oscillations in approaching the DKM ignition delay. We anticipate that the required number of constraints could be reduced by an in-situ adaptive tabulation strategy or by repeated use of our algorithm on a more local basis.

Finally, in Fig. 13 we show the different results that we may obtain with various variants of the proposed methodology, by choosing to minimize different measures of the distance between the actual $\boldsymbol{\Lambda}_{\rm DoD}(z_p)$ obtained with the DKM simulation and its RCCE approximation $\boldsymbol{\Lambda}_{\rm DoD}^{\rm RCCE}(z_p)$. Figure 13 compares the DKM results with the different RCCE simulations for the same number of constraints ($n_{\rm c} = 6$ in addition to $n_{\rm el} = 3$) obtained for the 900 K/10 bar ignition case with the different sets of constraints provided by four variants of the proposed algorithm – ASVDADD, ARREFADD(Mean), ARREFADD(Max), ARREFADD(sorted Max) – based on minimizing, respectively, $\delta_{\rm Fro}$ given by Eq. (50), δ given by Eq. (47), $\delta^{\max}$ given by the relation

$$\delta^{\max}(\varepsilon) = \frac{\max_{z_p}|\boldsymbol{\epsilon}^{\varepsilon}(z_p)|_2}{\max_{z_p}|\boldsymbol{\Lambda}_{\rm DoD}(z_p)|_2} = \frac{\frac{1}{P}\sum_{p=1}^{P}\left(\sum_{j=1}^{n_{\rm sp}}\left[\Lambda_{{\rm DoD}j}(z_p) - \Lambda_{{\rm DoD}j}^{{\rm RCCE}(\varepsilon)}(z_p)\right]^2\right)^{1/2}}{\frac{1}{P}\sum_{p=1}^{P}\left(\sum_{j=1}^{n_{\rm sp}}\left[\Lambda_{{\rm DoD}j}(z_p)\right]^2\right)^{1/2}} \tag{54}$$

and again $\delta^{\max}$ given by Eq. (54) but done after sorting the P samples of $\boldsymbol{\Lambda}_{\rm DoD}$ in ascending order of $|\boldsymbol{\Lambda}_{\rm DoD}|$.

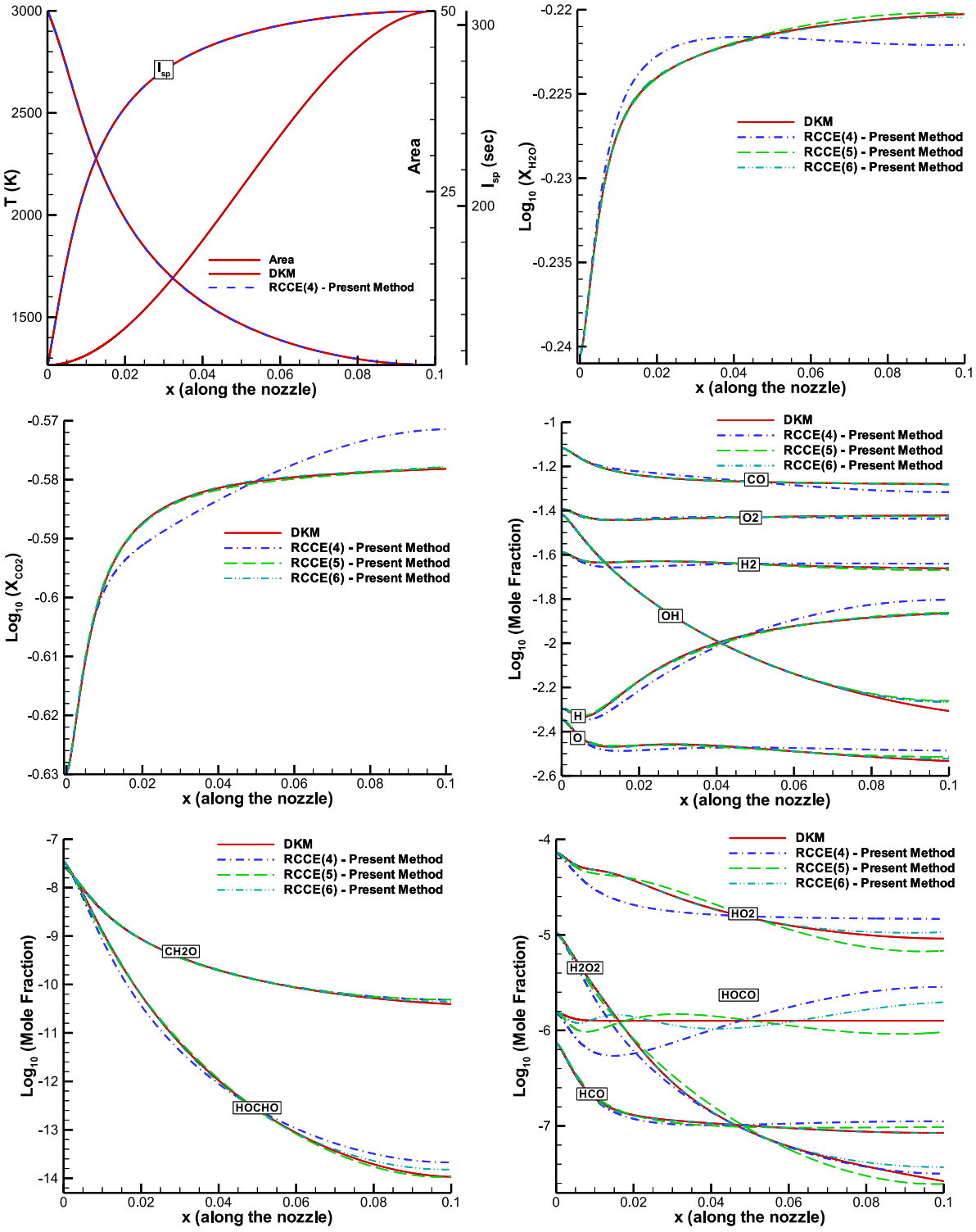

Fig. 10. Plots of temperature T, specific impulse I_{sp}, and mole fractions X_j of the main species versus dimensionless downstream axial distance x resulting from RCCE simulations compared with the corresponding data from the underlying DKM simulation, for the conditions detailed in Fig. 1 except for the nozzle length which here is 100 times shorter. Here the comparisons are for the products of methane oxycombustion, between the results of a 29 species/133 reactions DKM simulation and three RCCE simulations with 4, 5, and 6 total constraints. Constraints additional to the three elemental ones are obtained from the ARREFADD algorithm in this case.

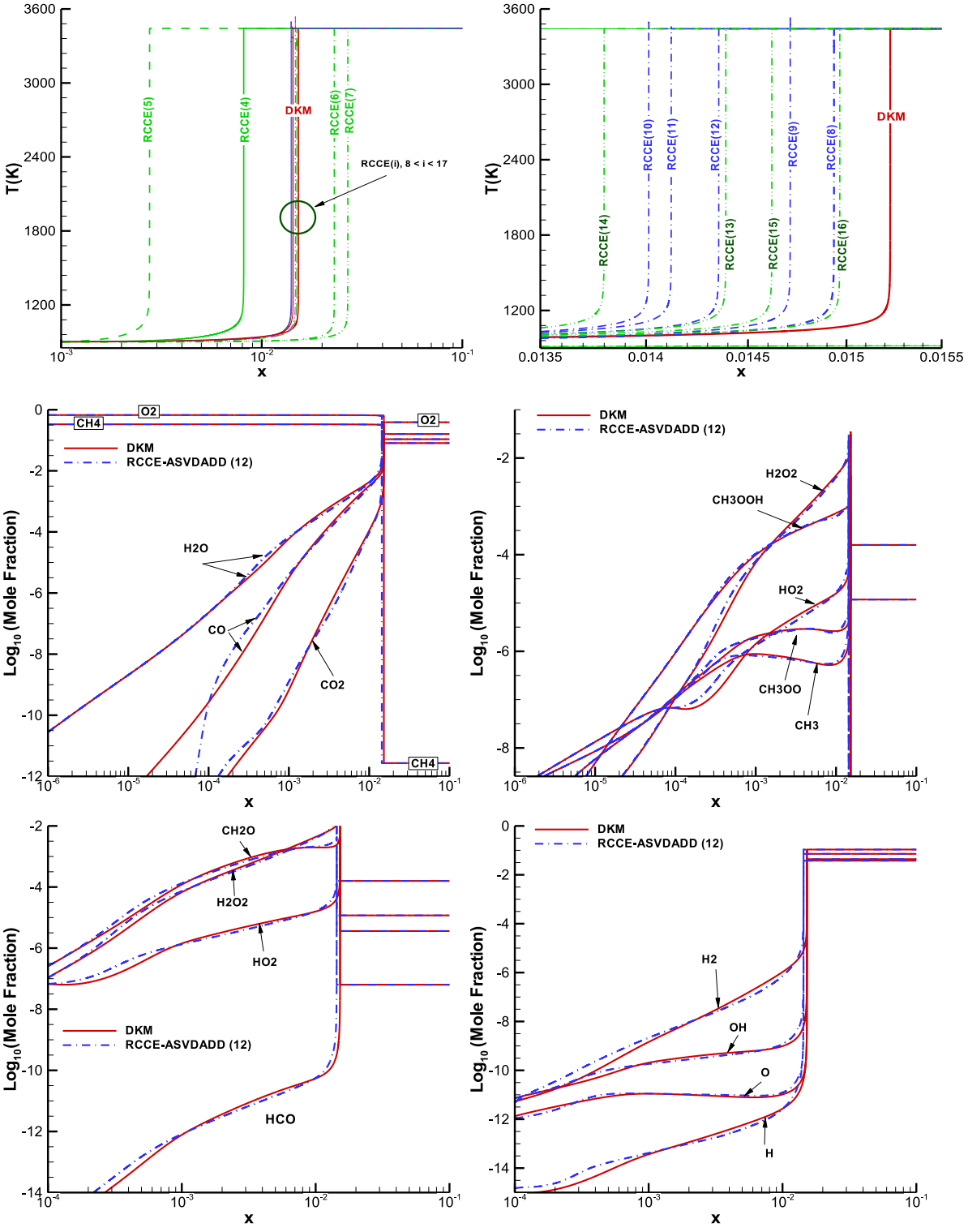

Fig. 11. Ignition of a stoichiometric mixture of methane and oxygen at 900 K and 10 bar in a subsonic constant area plug flow reactor. Comparison between the results of a 29 species/133 reactions DKM simulation and several RCCE simulations. Constraints additional to the three elemental ones are obtained from the ASVDADD algorithm in this case.

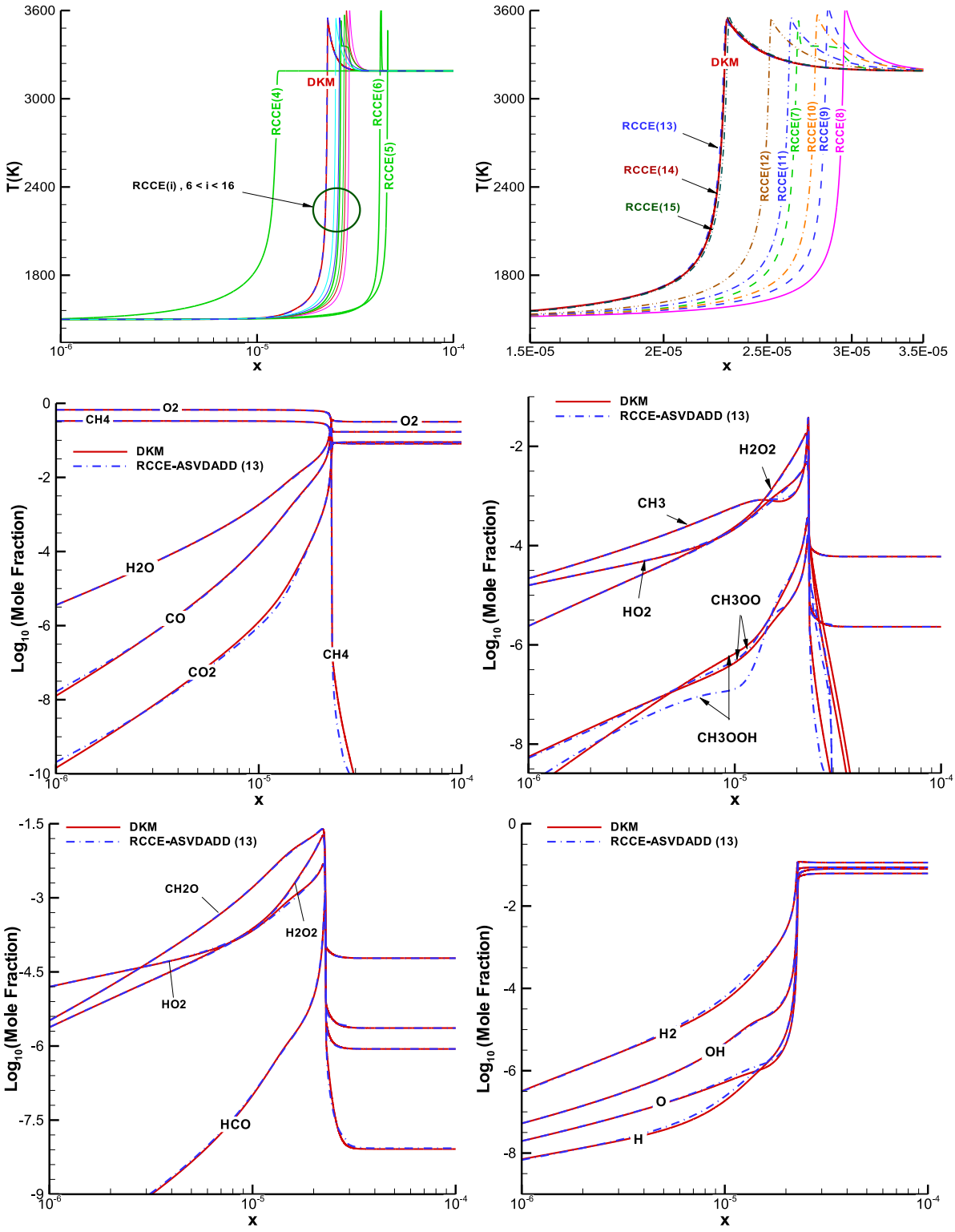

Fig. 12. Ignition of a stoichiometric mixture of methane and oxygen at 1500 K and 1 bar in a subsonic constant area plug flow reactor. Comparison between the results of a 29 species/133 reactions DKM simulation and several RCCE simulations. Constraints additional to the three elemental ones are obtained from the ASVDADD algorithm in this case.

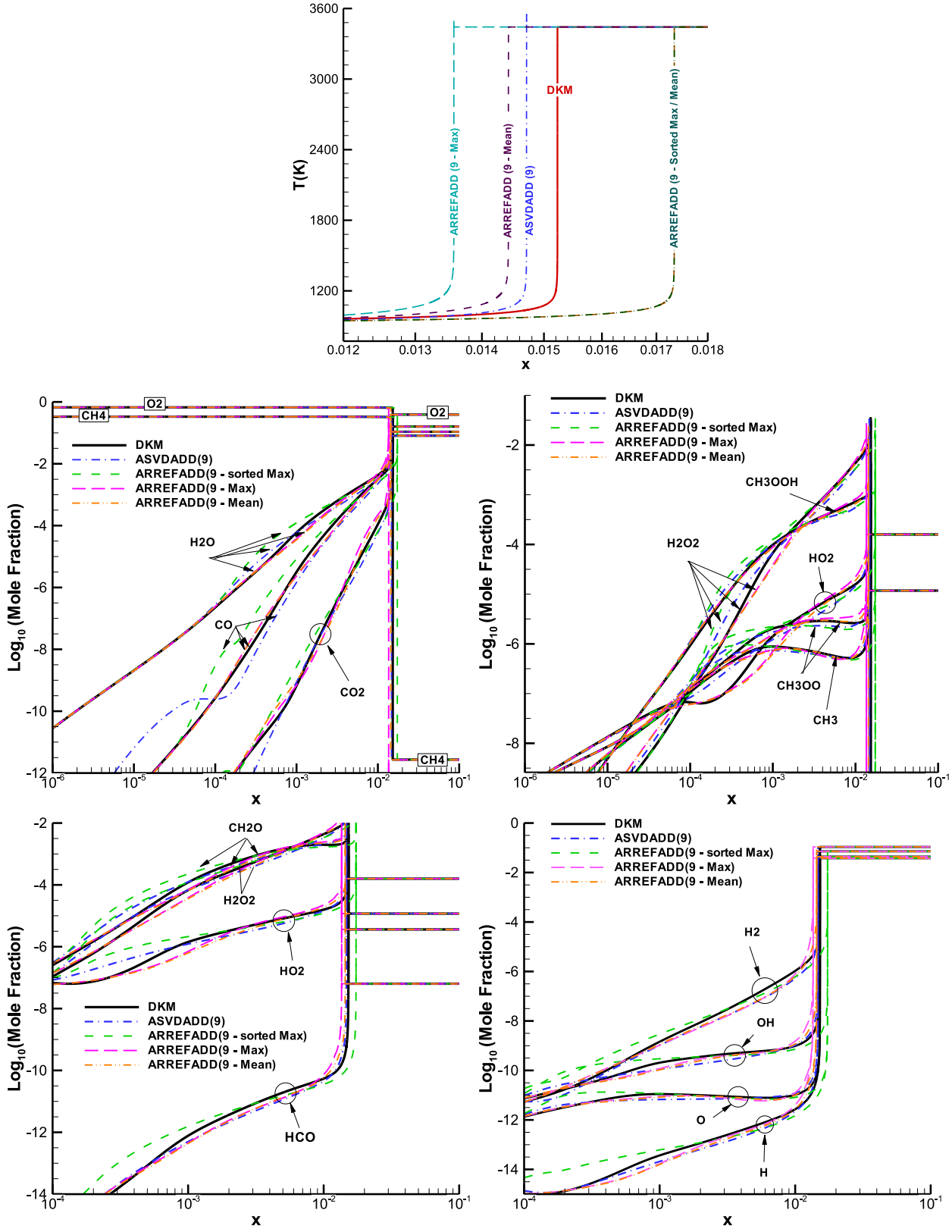

Fig. 13. Ignition of a stoichiometric mixture of methane and oxygen at 900 K and 10 bar in a subsonic constant area plug flow reactor. Comparison between the results of a 29 species/133 reactions DKM simulation and several RCCE simulations, all with sets of 9 constraints ($n_c = 6$ in addition to $n_{el} = 3$), but obtained by four variants of the proposed algorithm (see text).

10. Conclusions

The Rate-Controlled Constrained-Equilibrium (RCCE) method provides a strongly thermodynamically consistent, general model order reduction framework to model, with good degrees of approximation, complex chemical kinetics in applications involving shifting equilibrium, frozen equilibrium, as well as highly non-equilibrium kinetic problems. The method in general requires a significantly smaller number of differential equations than required by a full Detailed Kinetic Model (DKM). To provide accurate approximations, the method requires accurate identification of the bottleneck kinetic mechanisms responsible for slowing down the relaxation of the state of the system towards local chemical equilibrium. More precisely, the method requires that such bottleneck mechanisms be characterized by means of a set of representative constraints. So far, a weakness of the RCCE method has been the absence of a fully automatable, systematic algorithm capable to identify the best constraints for a given range of conditions and a required level of approximation.

In this paper we propose a new methodology for systematic RCCE constraint identification. The algorithm is based on analysing how the degrees of disequilibrium (DoD) of the chemical reactions behave in a full DKM test simulation. We call it ARREFADD because it is based on computing the Approximate Reduced Row Echelon Form of the Actual Degrees of Disequilibrium (ARREFADD) with respect to a preset tolerance level. Indeed, for each given range of conditions, any given DKM is characterized by a number of rate-limiting kinetic bottlenecks that is generally much smaller than the number of species in the model. As a result, the DoDs of all the chemical reactions effectively assemble into a small number of groups that bear the information of the rate-controlling constraints because the DoDs of all the reactions in each group exhibit almost identical behaviour (time evolution, spatial dependence). When the identification of these groups can be done by simple inspection, the RCCE constraints are obtained by means of a simple kernel analysis of a matrix constructed from the stoichiometric coefficients of subsets of reactions. When, as in most practical cases, the structure of the DoD traces is too complex to allow the grouping of reactions by simple inspection, the methodology can be still implemented by computing the approximate reduced row echelon form of the DoD traces, where the degree of approximation may be tuned by setting the tolerance level. Geometrically, the procedure identifies a low dimensional subspace in DoD space from which the actual DoD traces do not depart beyond a fixed distance related to the preset tolerance level.

The effectiveness of the methodology is demonstrated in several test cases of increasing complexity. For a one-dimensional study of expansion in a supersonic nozzle of the products of the oxy-combustion of hydrogen, the simple chemical kinetics (8 species, 24 reactions), the mild expansion rate, and the assumption of chemical equilibrium inlet conditions allow grouping by inspection: the analysis predicts and RCCE simulations confirm that, under the geometrical and boundary conditions considered, the underlying DKM is accurately represented by only two mathematically derived constraints, instead of the three constraints identified for the same problem in a recently published work also based on DoD analysis. When the expansion rate is much higher or the kinetic scheme is more complex (we consider methane/oxygen, 29 species, 133 reactions) the same supersonic nozzle expansion setup does not allow grouping by simple inspection of the DoD traces. Nevertheless, the ARREFADD algorithm easily identifies sets of constraints that make the RCCE simulations very accurate for very small numbers of constraints. The effectiveness of the method is also demonstrated for a more complex test case involving ignition of a homogeneous mixture of methane and oxygen.

In the spirit of typical multi-scale modelling approaches, as well as the Greedy and LOI algorithms, it is foreseen that the present constraint selection methodology can be used systematically to map (for example by in situ adaptive tabulation as already suggested in Ref. [38]) the range of conditions of interest in a given problem with a set of short DKM simulations to provide the DoD data needed by the ARREFADD constraint identification algorithm.

We conclude that the new constraint selection algorithm essentially resolves the difficulties that have prevented the RCCE method [1–14,39] from a more widespread use in reduced order modelling of detailed combustion kinetic models of hydrocarbon fuels. In addition, the ARREFADD model order reduction method can find natural extensions also in the more general field of nonequilibrium thermodynamics, for example in the general frameworks discussed in Ref. [40].

Acknowledgments

This paper was made possible by NPRP award 7-252-2-113 from the Qatar National Research Fund (a member of The Qatar Foundation). The statements made herein are solely the responsibility of the authors.

Appendix A. Simple implementation of the ARREFADD algorithm

The following very simple MatLab code implements the constraint selection methodology outlined in Section 7. It elaborates DKM data on DoDs that must be stored in a file named DoDsFromDKM.dat to generate a set of constraints for a prescribed tolerance threshold value ε to be assigned to the variable TOL. The stoichiometric matrix must be stored in a file named nu.dat. For the set tolerance threshold, the program returns the set of orthonormal vectors $\boldsymbol{a}_i$ that can be used as constraints according to Eq. (44).

```
clear all
close all
%
% read DoD data from DKM simulation
% from .dat file with one row for each
p=1,...,P
% and on each row: x_p DoD(x_1) ... DoD(x_n_r)
%
DoDdata=load('DoDsFromDKM.dat'); % P X 1+n_r
xp=DoDdata(:,1); % P X 1
DoDall=DoDdata(:,2:end); % P X n_r
%
% read matrix of stoichiometric coefficients
% from .dat file with one row for each reaction
% and on each row: nu_{1\ell} ... nu_{n_sp\ell}
%
nu=load('nu.dat'); % n_r X n_sp
nut=nu'; % n_sp X n_r
%
% find a basis for the lin span of the
% columns of matrix nut
% using standard MatLab function rref
%
[RREFnu,ibasisnut]=rref(nut);
% find rref of nut
r=length(ibasisnut); % rank of nu
%
% set of basis reactions and their DoDs
%
nuindep=nut(:,ibasisnut); % n_sp X r
DoDindep=DoDall(:,ibasisnut); % P X r
```

```
%
% compute the basis \theta_k with respect
% to which \Lambda_ODoD = sum_k \phi_k \theta_k
%
M=nuindep'*nuindep; % r X r
W=inv(M); % r X r
Theta=nuindep*W; % n_sp X r each column is a
\theta_k
%
% now we can compute \Lambda_ODoD
%
LambdaODoD=Theta*DoDindep'; % n_sp X P
%
% set a tolerance threshold level
%
TOL=1.205
%
% find constraints
%
[LambdaRREF,ibasisLambda] = rref(LambdaODoD,TOL);
nc = length(ibasisLambda)% rank of LambdaRREF
%
% basis for the approximate range of LambdaODoD
%
a=LambdaODoD(:,ibasisLambda); % n_sp x nc
%
% orthnormal basis
%
aorthonormal=orth(a) % n_sp x nc the columns
are our CONSTRAINTS
%
% compute the \gamma_i such that %
LambdaRCCE = \sum_i^nc \gamma_i a_i
%
gamma=LambdaODoD'*aorthonormal;
LambdaRCCE=aorthonormal*gamma';
%
% compute the corresponding approximate DoDs
%
DoDRCCE=nuindep'*LambdaRCCE;
%
% estimate of relative distance of Lambda from
span(a_i) %
Epsilon=LambdaODoD'-LambdaRCCE'; % M x 8
P=size(LambdaODoD,2);
normEpsilon=zeros(P,1);
normLambdaODoD=zeros(P,1);
for s=1:P normEpsilon(s)=norm(Epsilon(s,:));
normLambdaODoD(s)=norm(LambdaODoD(:,s));
end
delta=mean(normEpsilon)/mean(normLambdaODoD)
```

For example, the RCCE simulations shown in Fig. 4 are obtained by assuming the constraints determined by running the above MatLab code on the DKM-DoD data plotted in Fig. 2. Setting $\varepsilon = \mathrm{TOL} = 1.205$, the code yields the following orthonormal basis (aorthonormal) for the approximate range of $\Lambda_{\mathrm{DoD},jp}$:

$\boldsymbol{a}_1^{\varepsilon=1.205}$ $\boldsymbol{a}_2^{\varepsilon=1.205}$

```
-0.5334 -0.2156
 0.0352 -0.4827
-0.6463 -0.0159
-0.1921 -0.1038
-0.0789 -0.3066
 0.3759 -0.3944
-0.1917  0.5632
 0.2747  0.3778
```

and the resulting mean error $\delta = 0.312\%$. These are the two constraints (in addition to the two elemental ones) used to obtain the RCCE(4):PresentMethod plots shown in Fig. 4. As seen in the discussion of Fig. 5, without changing the number of constraints, we could further minimize the mean error to $\delta = 0.25\%$ by setting $\varepsilon = \mathrm{TOL} = 1.064$.

Again, setting $\varepsilon = \mathrm{TOL} = 6.6$ for the DKM-DoD data of Fig. 2, the orthonormal basis (aorthonormal) for the approximate range of $\Lambda_{\mathrm{DoD},jp}$ that obtains is

$\boldsymbol{a}_1^{\varepsilon=6.6}$

```
-0.5298
 0.0468
-0.6460
-0.1887
-0.0727
 0.3853
-0.2020
 0.2638
```

and the resulting mean error is $\delta = 4.06\%$. These is the single constraint (in addition to the two elemental ones) used to obtain the RCCE(3):PresentMethod plots shown in Fig. 4.

Again, the RCCE simulations shown in Fig. 9 are obtained by assuming the constraints determined by running the above MatLab code on the DKM-DoD data plotted in Fig. 7. Setting $\varepsilon = \mathrm{TOL} = 2.06$, the code yields the following orthonormal basis (aorthonormal) for the approximate range of $\Lambda_{\mathrm{DoD},jp}$

$\boldsymbol{a}_1^{\varepsilon=2.06}$ $\boldsymbol{a}_2^{\varepsilon=2.06}$

```
-0.5506 -0.2605
 0.0433 -0.4499
-0.6500 -0.0380
-0.1816 -0.0649
-0.0846 -0.3027
 0.3996 -0.2416
-0.1496  0.7508
 0.2241  0.1015
```

and the resulting mean error $\delta = 0.814\%$. These are the two constraints (in addition to the two elemental ones) used to obtain the RCCE(4):PresentMethod results shown in Fig. 4. As seen in the discussion of Fig. 5, without changing the number of constraints, we could further minimize the mean error to $\delta = 0.807\%$ by setting $\varepsilon = \mathrm{TOL} = 2.142$.

Again, setting $\varepsilon = \mathrm{TOL} = 9.2772$ for the DKM-DoD data of Fig. 7, the orthonormal basis (aorthonormal) for the approximate range of $\Lambda_{\mathrm{DoD},jp}$ that obtains is

$\boldsymbol{a}_1^{\varepsilon=9.2772}$

```
-0.5491
 0.0442
-0.6500
-0.1814
-0.0837
 0.3970
-0.1551
 0.2289
```

and the resulting mean error is $\delta = 4.025\%$. These is the single constraint (in addition to the two elemental ones) used to obtain the RCCE(3):PresentMethod results shown in Fig. 9.

Setting $\varepsilon = \mathrm{TOL} = 0.7003$, the orthonormal basis (aorthonormal) for the approximate range of $\Lambda_{\mathrm{DoD},jp}$ that obtains is

$\boldsymbol{a}_1^{\varepsilon=0.7003}$ $\boldsymbol{a}_2^{\varepsilon=0.7003}$ $\boldsymbol{a}_3^{\varepsilon=0.7003}$

```
-0.5522  0.2587  0.0713
 0.0412  0.4094  0.1690
-0.6500  0.0323 -0.0104
```

```
-0.1823   0.0589   0.0032
-0.0855   0.2722   0.1838
 0.4009   0.1106   0.5802
-0.1439  -0.8168   0.1670
 0.2211   0.0866  -0.7536
```

Appendix B. Simple implementation of the ASVDADD variant

The following MatLab code implements the even simpler constraint selection methodology outlined in Section 8. We removed comments from the first part of the code that is identical to that given in Appendix A.

```
clear all
close all
DoDdata=load('DoDsFromDKM.dat'); % P X 1+n_r
xp=DoDdata(:,1); % P X 1
DoDall=DoDdata(:,2:end); % P X n_r
nu=load('nu.dat'); % n_r X n_sp
nut=nu'; % n_sp X n_r
[RREFnu,ibasisnut]=rref(nut); % find rref of
nut
r=length(ibasisnut); % rank of nu
nuindep=nut(:,ibasisnut); % n_sp X r
DoDindep=DoDall(:,ibasisnut); % P X r
M=nuindep'*nuindep; % r X r
W=inv(M); % r X r
Theta=nuindep*W; % n_sp X r each column is a
\theta_k
LambdaODoD=Theta*DoDindep'; % n_sp X P
%
% find the SVD % using standard MatLab function
svd
%
[U,S,V]=svd(LambdaODoD);
%
r=rank(S);
sigma=diag(S);
%
% compute errors
%
for n=1:r
deltaFro(n)=norm(sigma(n:end))/norm(sigma);
end
delta2=diag(S)/S(1,1);
%
% show results
%
Best_candidates_for_RCCE_constraints=U(:,1:r)
Corresponding_errors_neglecting_contraints_
beyond_nc=(1:r)
Delta2=[delta2(2:r);0]'
DeltaFro=[deltaFro(2:r)';0]'
```

The result of running this code for the DKM-DoD data of Fig. 2 is the following:

```
  Best_candidates_for_RCCE_constraints =
-0.5497 -0.2645   0.0078   0.1956   0.5558 -0.4200
 0.0443 -0.4277   0.1733 -0.5222 -0.1480   0.2716
-0.6499 -0.0397   0.0131 -0.1796 -0.6336 -0.1950
-0.1817 -0.0646   0.0063 -0.3382   0.4758   0.4531
-0.0833 -0.2810   0.1446   0.7353 -0.1857   0.4845
 0.4002 -0.1519   0.5607   0.0194 -0.0168 -0.4805
-0.1520   0.7992   0.2321   0.0122   0.0413   0.1074
 0.2242 -0.0228 -0.7619   0.0349 -0.0699 -0.1711
Corresponding_errors_neglecting_contraints_
beyond_nc
i.e.,for nc =   1        2        3        4        5        6
Delta2 =      0.0329   0.0064   0.0009   0.0002   0.0001   0
DeltaFro =    0.0336   0.0064   0.0010   0.0002   0.0001   0
```

It is noteworthy that these results are close, but not identical to those obtained in Appendix A, due to the different measures of approximation minimized by the ARREFADD and the ASVDADD variants of the method.

Appendix C. Vector notation

The use of vector space formulations and notions in chemical kinetics and model reduction has proved to be expedient not only for compacting the notation but also for exploiting many relevant theorems from linear algebra. However, various authors use different notations and levels of abstraction. In this paper, for simplicity, we adopt a low level of abstraction because to understand the proposed ARREFADD algorithm it suffices to consider a generic n-dimensional real vector space $\mathbb{R}^n$ consisting of all ordered n-tuples of real numbers, such as $\boldsymbol{x} = [x_1 \ \dots \ x_n]$ and $\boldsymbol{y} = [y_1 \ \dots \ y_n]$, equipped with the scalar product $\langle \boldsymbol{x} | \boldsymbol{y} \rangle = \sum_{i=1}^{n} x_i y_i$. In particular, the vectors $\mathbf{N} = [N_1 \ \dots \ N_{n_{\rm sp}}]$, $\boldsymbol{\Lambda} = [\lambda_1 \ \dots \ \lambda_{n_{\rm sp}}]$, $\boldsymbol{\nu}_\ell = [\nu_{1\ell} \ \dots \ \nu_{n_{\rm sp}\ell}]$ for each fixed ℓ, $\boldsymbol{a}_i = [a_{i1} \ \dots \ a_{in_{\rm sp}}]$ for each fixed i, $\boldsymbol{\chi}_k = [\chi_{1k} \ \dots \ \chi_{n_{\rm sp}k}]$ for each fixed k, $\boldsymbol{\Lambda}_{\rm DoD}(z_p)$ for each fixed z_p, can all be viewed as elements of $\mathbb{R}^{n_{\rm sp}}$.

We also consider several $n \times m$ matrices: the $n_{\rm sp} \times n_{\rm r}$ matrix $\boldsymbol{\nu}$ of stoichiometric coefficients, the $n_{\rm c} \times n_{\rm sp}$ matrix $\boldsymbol{a}$ of constraint coefficients, the $n_{\rm sp} \times r$ matrix $\boldsymbol{\chi}$, the $r \times r$ matrix $\boldsymbol{M}$ and its inverse $\boldsymbol{W}$, the $n_{\rm sp} \times P$ matrix $\boldsymbol{\Lambda}_{\rm DoD}(z_p)$.

References

[1] J.C. Keck, D. Gillespie, Rate-controlled partial-equilibrium method for treating reacting gas mixtures, Combust. Flame 17 (1971) 237–241.

[2] J.C. Keck, Rate-controlled constrained equilibrium method for treating reactions in complex systems, in: R.D. Levine, M. Tribus (Eds.), The Maximum Entropy Formalism, MIT Press, Cambridge, MA, 1979, pp. 219–245. Available online: http://www.jameskeckcollectedworks.org/.

[3] G.P. Beretta, J.C. Keck, The constrained-equilibrium approach to nonequilibrium dynamics, in: R.A. Gaggioli (Ed.), Second Law Analysis and Modeling, ASME Book H0341C-AES, vol. 3, ASME, New York, 1986, pp. 135–139. Available online: http://www.jameskeckcollectedworks.org/.

[4] R. Law, M. Metghalchi, J.C. Keck, Rate-controlled constrained equilibrium calculations of ignition delay times in hydrogen–oxygen mixtures, Symp. (Int.) Combust. 22 (1988) 1705–1713.

[5] J.C. Keck, Rate-controlled constrained-equilibrium theory of chemical reactions in complex systems, Prog. Energy Combust. Sci. 16 (1990) 125–154.

[6] P. Bishnu, D. Hamiroune, H. Metghalchi, J.C. Keck, Constrained-equilibrium calculations for chemical systems subject to generalized linear constraints using the NASA and STANJAN equilibrium programs, Combust. Theory Model. 1 (1997) 295–312.

[7] D. Hamiroune, P. Bishnu, H. Metghalchi, J.C. Keck, Rate-controlled constrained-equilibrium method using constraint potentials, Combust. Theory Model. 2 (1998) 81–94.

[8] P. Bishnu, D. Hamiroune, H. Metghalchi, Development of constrained equilibrium codes and their applications in nonequilibrium thermodynamics, ASME J. Energy Res. Technol. 123 (2001) 214–220.

[9] S. Ugarte, Y. Gao, H. Metghalchi, Application of the maximum entropy principle in the analysis of a non-equilibrium chemically reacting mixture, Int. J. Thermodyn. 8 (2005) 43–53.

[10] M. Janbozorgi, H. Metghalchi, Rate-controlled constrained-equilibrium theory applied to expansion of combustion products in the power stroke of an internal combustion engine, Int. J. Thermodyn. 12 (2009) 44–50.

[11] M. Janbozorgi, S. Ugarte, H. Metghalchi, J.C. Keck, Combustion modelling of mono-carbon fuels using the rate-controlled constrained-equilibrium method, Combust. Flame 156 (2009) 1871–1885.

[12] G.P. Beretta, J.C. Keck, M. Janbozorgi, H. Metghalchi, The rate-controlled constrained-equilibrium approach to far-from-local-equilibrium thermodynamics, Entropy 14 (2012) 92–130.

[13] G. Nicolas, M. Janbozorgi, H. Metghalchi, Constrained-equilibrium modeling of Methane oxidation in air, ASME J. Energy Res. Technol. 136 (2014) 032205.
[14] G. Nicolas, H. Metghalchi, Comparison between RCCE and shock tube ignition delay time at low temperatures, ASME J. Energy Res. Technol. 137 (2015) 062203.
[15] V. Yousefian, A rate-controlled constrained-equilibrium thermochemistry algorithm for complex reacting systems, Combust. Flame 115 (1998) 66–80.
[16] V. Hiremath, Z. Ren, S.B. Pope, A greedy algorithm for species selection in dimension reduction of combustion chemistry, Combust. Theory Model. 14 (2010) 619–652.
[17] V. Hiremath, Z. Ren, S.B. Pope, Combined dimension reduction and tabulation strategy using ISAT-RCCE-GALI for the efficient implementation of combustion chemistry, Combust. Flame 158 (2011) 2113–2127.
[18] S. Rigopolous, T. Lovas, A LOI-RCCE methodology for reducing chemical kinetics, with application to laminar premixed flames, Proc. Combust. Inst. 32 (2009) 569–576.
[19] M. Janbozorgi, H. Metghalchi, Rate-controlled constrained-equilibrium modeling of H–O reacting nozzle flow, J. Propul. Power 28 (2012) 677–684 with the following errata corrigenda: $\nu_{jk} = \nu_{jk}^{-} - \nu_{jk}^{+}$, $E_T = C_p T + \sum_{j=1}^{n_s} [N_j] M_j h_j e_j / RT$, $E_u = \sum_{j=1}^{n_s} [N_j] M_j (h_j + u^2)$.
[20] S.W. Benson, The induction period in chain reactions, J. Chem. Phys. 20 (1952) 1605.
[21] U. Mass, S.B. Pope, Simplifying chemical kinetics: Intrinsic low-dimensional manifolds in composition space, Combust. Flame 88 (1992) 239–264.
[22] S.H. Lam, D.A. Goussis, Understanding complex chemical kinetics with computational singular perturbation, Proc. Combust. Inst. 22 (1988) 931–941.
[23] S.H. Lam, Using CSP to understand complex chemical kinetics, Combust. Sci. Technol. 89 (1993) 375–404.
[24] V. Mauro, F. Creta, D.A. Goussis, J.C. Lee, H.N. Najm, An automatic procedure for the simplification of chemical kinetic mechanisms based on CSP, Combust. Flame 146 (2006) 29–51.
[25] D.A. Schwer, P. Lu, W.H. Green, An adaptive chemistry approach to modeling complex kinetics in reacting flows, Combust. Flame 133 (2003) 451–465.
[26] I. Banerjee, M.G. Ierapetritou, An adaptive reduction scheme to model reactive flow, Combust. Flame 144 (2006) 619–633.
[27] O. Oluwole, B. Bhattacharjee, J.E. Tolsma, P.I. Barton, W.H. Green, Rigorous valid ranges for optimally reduced kinetic models, Combust. Flame 146 (2006) 348–365.
[28] M. Rein, The partial-equilibrium approximation in reacting flows, Phys. Fluids A 4 (1992) 873 (see also the Erratum, Phys. Fluids A (1992) 2930).
[29] T. Lu, C.K. Law, Linear time reduction of large kinetic mechanisms with directed relation graph: n-heptane and iso-octane, Combust. Flame 144 (2006) 24–36.
[30] Z. Ren, S.B. Pope, A. Vladimirsky, J.M.J. Guckenheimer, The invariant constrained equilibrium edge pre-image curve method for the dimension reduction of chemical kinetics, J. Chem. Phys. 124 (2006) 114111.
[31] A.N. Gorban, I.V. Karlin, Method of invariant manifold for chemical kinetics, Chem. Eng. Sci. 58 (2003) 4751.
[32] T. Lovas, Automatic generation of skeletal mechanisms for ignition combustion based on level of importance analysis, Combust. Flame 156 (2009) 1348–1358.
[33] M. Kooshkbaghi, C.E. Frouzakis, K. Boulouchos, I.V. Karlin, Entropy production analysis for mechanism reduction, Combust. Flame 161 (2014) 1507.
[34] G.P. Beretta, E.P. Gyftopoulos, What is a chemical equilibrium state? ASME J. Energy Res. Technol. 137 (2015) 021008.
[35] G.P. Beretta, E.P. Gyftopoulos, Thermodynamic derivations of conditions for chemical equilibrium and of Onsager reciprocal relations for chemical reactors, J. Chem. Phys. 121 (2004) 2718–2728.
[36] C.D. Martin, M.A. Porter, The extraordinary SVD, Am. Math. Mon. 119 (2012) 838–851.
[37] S. Wold, K. Esbensen, P. Geladi, Principal component analysis, Chemom. Intell. Lab. Syst. 2 (1987) 37–52.
[38] S. Pope, Identification, tabulation and use of low-dimensional manifolds for combustion computations, 9th International Conference on Numerical Combustion, Sorrento, 7–10 April, 2002 paper MS023.
[39] F. Hadi, M.R.H. Sheikhi, A comparison of constraint and constraint potential forms of the rate-controlled constrained-equilibrium method, ASME J. Energy Res. Technol. 138 (2016) 022202.
[40] G.P. Beretta, Steepest entropy ascent model for far-nonequilibrium thermodynamics: unified implementation of the maximum entropy production principle, Phys. Rev. E 90 (2014) 042113.